SANDIA REPORT

SAND97-1652 • UC-122
Unlimited Release
Printed September 1997

Finite Element Analysis of Sucker Rod Couplings with Guidelines for Improving Fatigue Life

Edward L. Hoffman

Prepared by
Sandia National Laboratories
Albuquerque, New Mexico 87185 and Livermore, California 94550

Sandia is a multiprogram laboratory operated by Sandia Corporation, a Lockheed Martin Company, for the United States Department of Energy under Contract DE-AC04-94AL85000.

Approved for public release; distribution is unlimited.

Sandia National Laboratories

Issued by Sandia National Laboratories, operated for the United States Department of Energy by Sandia Corporation.

Available to DOE and DOE contractors from
Office of Scientific and Technical Information
P.O. Box 62
Oak Ridge, TN 37831

Prices available from (615) 576-8401, FTS 626-8401

Available to the public from
National Technical Information Service
U.S. Department of Commerce
5285 Port Royal Rd
Springfield, VA 22161

NTIS price codes
Printed copy: A04
Microfiche copy: A01

SAND97-1652
Unlimited Release
Printed September 1997

Distribution
Category UC-122

Finite Element Analysis of Sucker Rod Couplings with Guidelines for Improving Fatigue Life

Edward L. Hoffman
Engineering and Structural Mechanics Division
Sandia National Laboratories
Albuquerque, New Mexico 87185

Abstract

The response of a variety of sucker rod couplings to an applied axial load was simulated using axisymmetric finite element models. The calculations investigated three sucker rod sizes and various combinations of the slimhole, Spiralock, and Flexbar modifications to the coupling. In addition, the effect of various make-ups (assembly tightness) on the performance of coupling was investigated. The make-up process, based on measured circumferential displacement of the coupling from a hand-tight position, was simulated by including a section of an axially expanding material in the box section which, when heated, produced the desired mechanical interference which would result from making-up the coupling. An axial load was applied to the sucker rod ranging from -5 ksi to 40 ksi, encompassing three load cycles identified on a modified Goodman diagram as acceptable for indefinite service life of the sucker rods. The simulations of the various coupling geometries and make-ups were evaluated with respect to how well they accomplish the two primary objectives of preloading threaded couplings: (1) to lock the threaded coupling together so that it will not loosen and eventually uncouple, and (2) to improve the fatigue resistance of the threaded connection by reducing the stress amplitude in the coupling when subjected to cyclic loading. A coupling will remain locked as long as the mating surfaces of the pin and box sections remain in compression, resisting rotational motion or loosening. The fatigue evaluation was accomplished in two parts: nominally and locally. In the nominal evaluation, a set of equations based on the gross dimensions of the coupling were derived which describe how a load applied to a sucker rod is distributed throughout a preloaded coupling. The local fatigue evaluation characterized the fatigue performance of the various couplings using the local stresses predicted in the finite element simulations and a stress equivalencing criterion for multiaxial stress states. This criterion is based on Sines' equivalent stress theory which states that the permissible effective alternating stress is a linear function of the mean hydrostatic stress. Perhaps the most significant finding in this study was the characterization of the coupling parameters which affect these two stress measures. The mean hydrostatic stress, which determines the permissible effective alternating stress, is a function of the coupling make-up. Whereas, the alternating effective stress is a function of the relative stiffnesses of the pin and box sections of the coupling and, as long as the coupling does not separate, is unaffected by the amount of circumferential displacement applied during make-up. The results of this study suggest approaches for improving the fatigue resistance of sucker rod couplings.

Contents

Figures

Tables

1 Introduction

Oil and gas production in the US has reached a point where significant effort is required to forestall declining production and stop the abandonment of significant unproduced resources. New technology developments are needed. However, because lifting costs are high relative to oil prices, the petroleum industry is downsizing and investing less effort in the development of new technology. The goal of Sandia National Laboratories' Applied Production Technology (APT) project is to extend the life of marginally economic wells by reducing the negative impacts of persistent production problems. The approach is to use "Sandia Technology" to rapidly diagnose industry-defined production problems and then propose or develop improved technology utilizing the capabilities of industry. One task of the APT project is the investigation of sucker rod and sinkerbar failures. Sucker rods and sinker bars are the primary components of rod pumping systems, the most common artificial lift technology utilized in domestic oil production. Thus, high sucker rod failure rates have a large economic impact on the domestic oil industry and threaten the domestic oil reserves with high abandonment rates. If the level of technology and understanding of the rod pumping system can be increased, there will be significant benefit to both the domestic industry and domestic energy security.

A sucker rod pump, illustrated in Figure 1, brings underground oil to the earth's surface. The primary drive motor turns a flywheel with a crank arm. Attached to the crank arm is a Pitman Arm which links the crank to the *walking beam*. The walking bean is a lever arm which pivots at its midsection. At the other end of the walking beam is the *horsehead*. A hanger cable hangs off the horsehead and is clamped to the rod string. This mechanism converts the rotary motion of the drive motor to a translational pumping motion. Two valves are used to maintain the direction of flow. A traveling valve, often just a ball in a cage, is attached to a plunger at the end of the rod string. At the base of the well is a stationary valve (another ball in a cage) called a standing valve.

The rod string, capable of reaching lengths of over 10,000 ft, consists of individual sections of steel rods called sucker rods. Sucker rods come in lengths ranging from 25 to 30 ft and

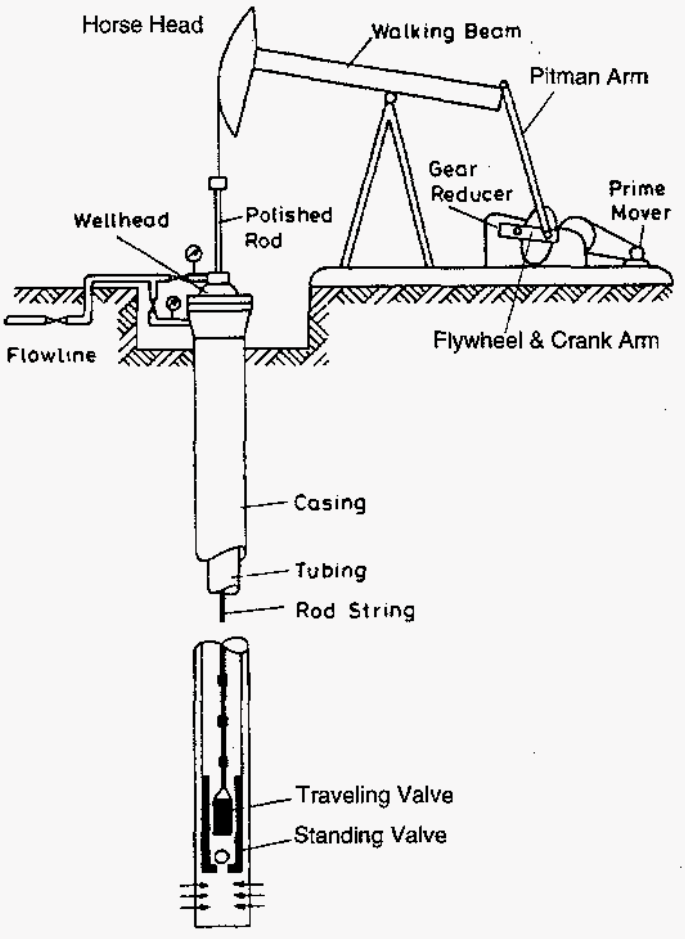

Figure 1. Illustration of sucker rod pump.

nominal diameters ranging from 0.5 to 1.125 inches. Each rod contains a threaded pin at each end as shown in Figure 2. Threaded couplings, known as *boxes*, are used to connect the sucker rods to produce the rod string. These pin and box coupling are tightened to a specified preload, known as the joint *make-up*, so that it will not loosen during normal operation.

In addition to supporting the pumping forces, each sucker rod must be strong enough to support the weight of the rods below it. Hence, loads are greater on the sucker rods farther up the rod string. The diameter of each sucker rod is specified by the well designer based on the strength of the rod material and the loads it will be exposed to. As most rod strings are made up of a single material, the resulting optimized rod string tapers down in diameter with distance down the well. Because the rod string is extremely long relative to its diameter, elastic stability of this long slender column is of concern to pump designers. The rod string must translate the force to the pump in *both* stroke directions. Because the entire length of the rod string will be in tension on the upward stroke, elastic stability of the rod string is not a problem. Furthermore, if the weight of the rod string exceeds the required pumping force on the downward stroke (as it typically does), then the upper sucker rods will also be in tension on the downward stroke. The lower rods, on the other hand, will be in compression on the downstroke, a condition which could result in downstroke compression buckling of the lower rods. To keep the rod string straight and in tension throughout the pump cycle, a section of large diameter bar, known as a *sinker bar*, is placed just above the pump. The sinker bar, typically consisting of large-diameter sucker rods (such as 7/8 or 1-inch), replaces an equal length of sucker rods immediately above the pump. This large diameter section of the rod string is both heavy enough to keep the sucker rods in tension and stiff enough to resist buckling. The sinker bar may also increase pump plunger overtravel (on the downstroke) which increases fluid production.

Rod string failures are very expensive to repair since the entire string must be disassembled and removed to access the failed rod. The rod string must then be reassembled. Wells with low production rates may not warrant the cost of repairing a failed rod. To maximize system reliability, safety and simplify system design, nearly every aspect of sucker rod system design, manufacturing and assembly has been standardized by the American Petroleum Institute (API). Because sucker rods are exposed to cyclic stresses, they are at risk of fatigue failure. Fatigue is the process of cumulative damage caused by repeated fluctuating loads whose magnitude is well below the material's ultimate strength under monotonic loading. To ensure a long fatigue life of the sucker rods, the API uses the modified Goodman stress diagram

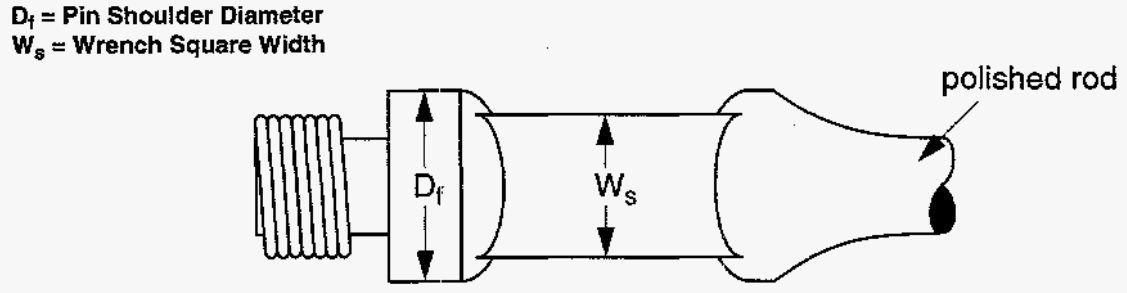

Figure 2. Threaded pin and shoulder at each end of the sucker rod.

(shown in Figure 3) to determine the allowable range of stress for a sucker rod. Based on the ultimate tensile strength of the material, the modified Goodman diagram defines a stress envelope (shaded area) within which a structural component can operate such that it will provide an infinite service life. Using this system, the well designer can determine the appropriate rod diameter based on a knowledge of the minimum load (on the downstroke) and the maximum load (on the upstroke). The modified Goodman diagram provides the fundamental rating which can be used where corrosion is not a factor. Since all well fluids are corrosive to some degree, the stress values determined from this diagram must be adjusted by an appropriate service factor based on the severity of the corrosion.

In spite of the thorough efforts of the API to ensure performance within the fatigue limits of the selected materials, sucker rod failures still occur. Pin failures comprise a large fraction of all rod pumped system failures. Not much is known about the performance of sucker rod couplings as they have not been extensively studied in the past. Because the coupling diameter is much larger than that of the rod, it has been assumed that the oversized coupling falls within the stress range specified by the Goodman diagram for the rod. This may not be true as the coupling is a complex preloaded mechanism which will react differently to axial loads than a solid rod. This report documents finite element simulations of the sucker rod coupling which were performed to provide a better understanding of sucker rod couplings and attempt to explain pin failures. All of the simulations were performed with JAC2D [1], a quasistatic finite element analysis code developed at Sandia National Laboratories.

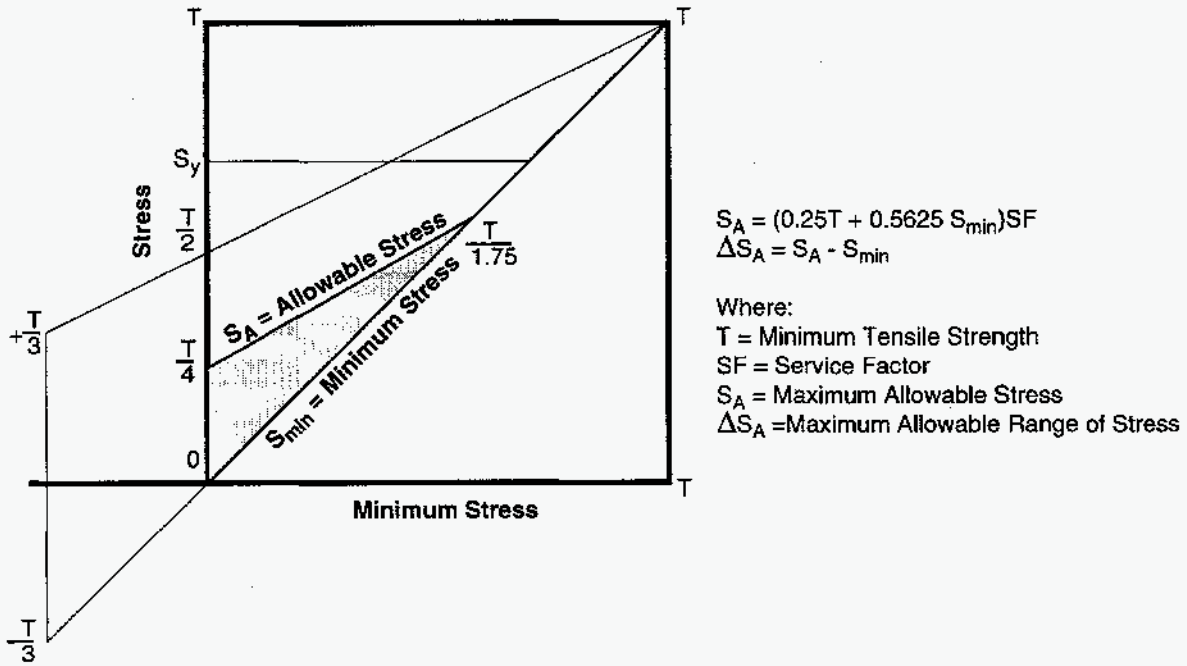

Figure 3. Modified Goodman diagram for allowable stress and range of stress for sucker rods in non-corrosive service.

2 Analysis Model

2.1 Finite Element Model of the Coupling Geometry

Detailed illustrations of the 7/8-inch coupling, with dimensions of the coupling and threads, are shown in Figure 4. An axisymmetric finite element representation of the sucker rod coupling is shown in Figure 5 with the axis of symmetry on the left side of the model. Although the threaded connection is a three-dimensional geometry, it can be adequately represented with an axisymmetric model since the thread pitch is small relative to the other dimensions of the coupling. Because the lower boundary of the box section is modeled with a symmetry plane, the model represents the coupling of two rods. The pin is modeled up to the shoulder and does not include the narrower rod section. This simplification was made to avoid modeling the asymmetric wrench flats which are located between the rod and the coupling shoulder. Since the applied loads are specified (from the Goodman plots) as stresses in the rod, the resulting stress at the larger diameter coupling shoulder was required as input into the model. This was accomplished by specifying a pressure multiplier equal to the ratio of the rod area to the shoulder area.

Four existing sucker rod designs and five proposed design modifications were the subjects of this computational study. The various sucker rod pin designs and proposed pin modifications are shown in Figure 6. The four existing sucker rod couplings studied here include the standard couplings for 3/4, 7/8, and 1-inch sucker rods. In addition, a 7/8-inch slimhole

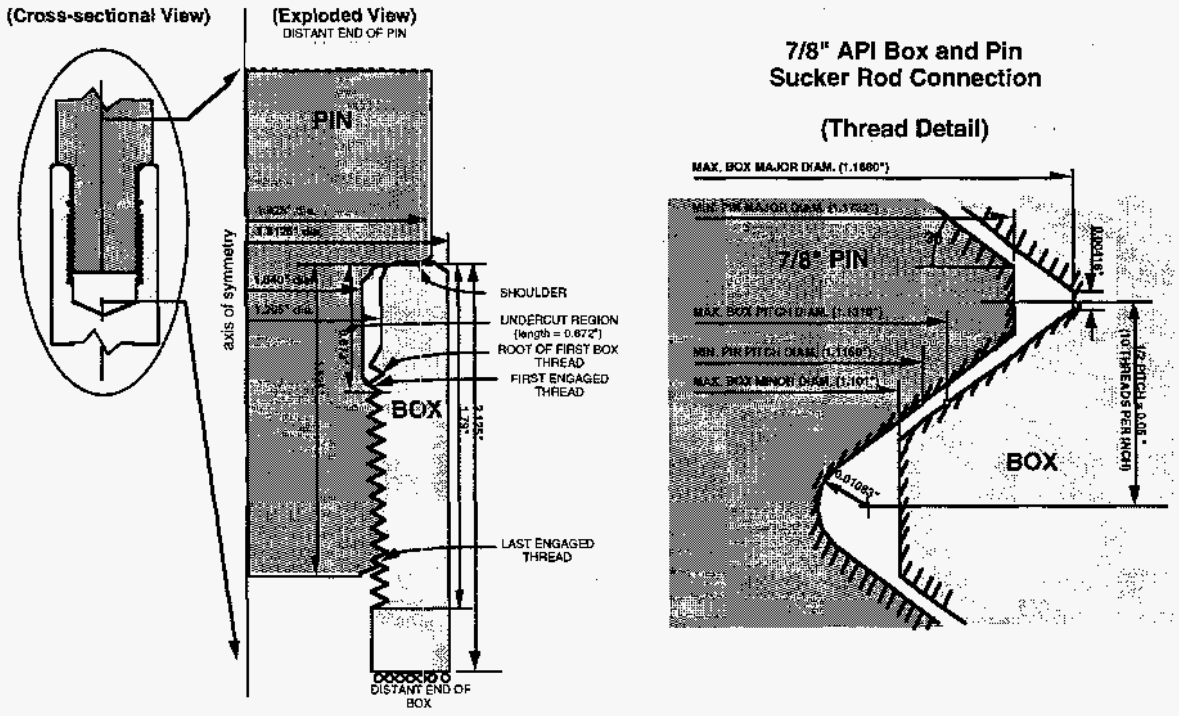

Figure 4. Detailed illustrations of the 7/8-inch coupling, with dimensions of the coupling and the threads.

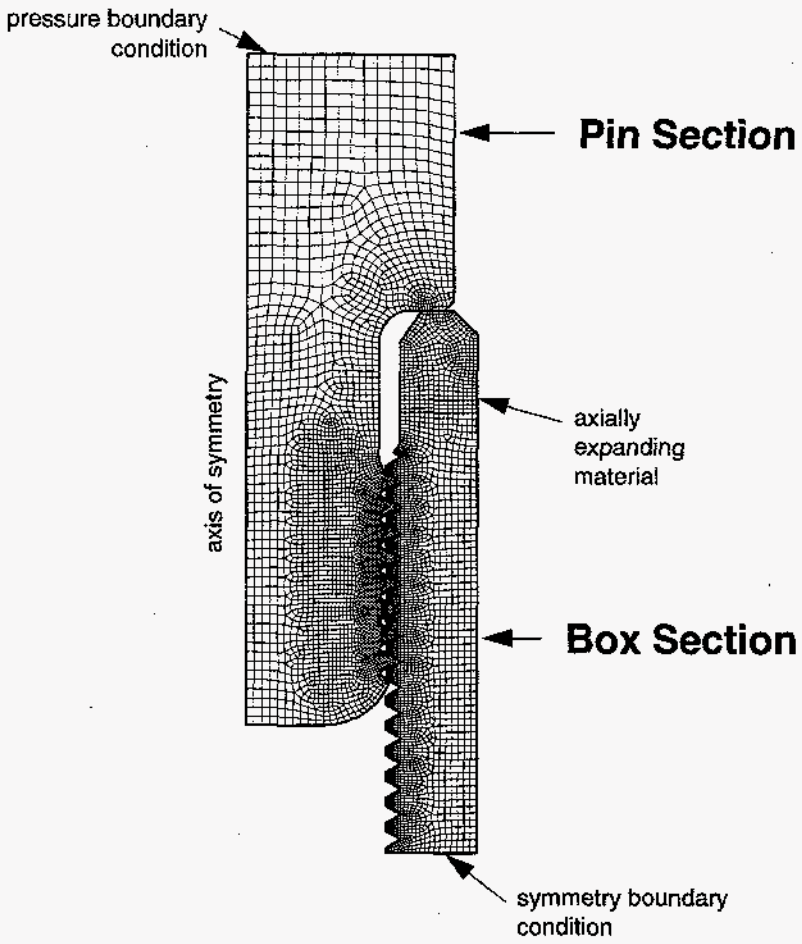

Figure 5. Axisymmetric finite element model of 7/8 inch sucker rod coupling, showing the pin and box sections.

coupling, used in applications of low well bore clearance, is also studied. The five modified geometries are variations of two basic modifications: the Flexbar pin, and Spiralock box. The Flexbar pin uses the same coupling as the standard sucker rod coupling designs. However, the pin is slightly longer and incorporates a shoulder on which the coupling rests. The second modification consists of a proprietary thread design, called Spiralock threads, which are used in the box section of the coupling. The pin retains the standard API threads in this configuration.

2.2 Preload of Sucker Rod Couplings

The API sucker rod tables contain recommendations for the assembly or preloading of sucker rod couplings, also known as *make-up*. The recommendations are based on a circumferential displacement, measured at the shoulder of the sucker rod, while tightening from a hand-tight position. These recommendations are summarized in Table 1 for the 3/4, 7/8, and 1-inch diameter sucker rods. The axial displacement of the pin (or interference at the shoulder) can be calculated as:

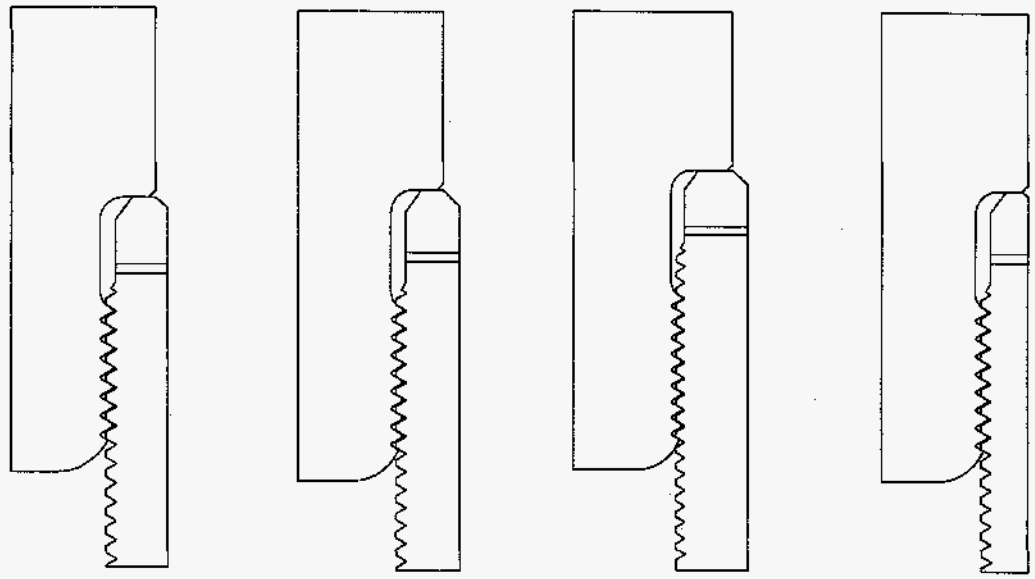

(a) Existing Sucker Rod Coupling Designs

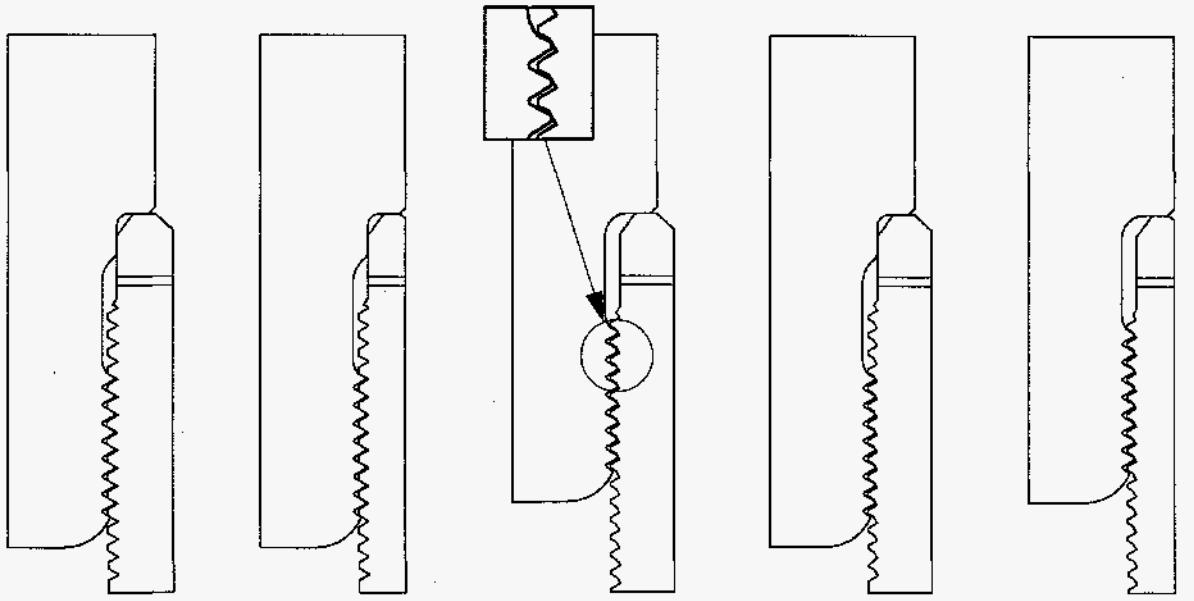

(b) Proposed Modifications to Sucker Rod Coupling Designs

Figure 6. Existing sucker rod coupling designs and proposed design modifications under investigation.

$$d_i = \frac{P d_c}{\pi D_f} \tag{1}$$

where P is the thread pitch, d_c is the circumferential displacement, and D_f is the shoulder diameter. All of the sucker rod sizes listed in Table 1 have a thread pitch of 0.1 inches. Simulating the preloading of the threaded coupling posed a particularly difficult problem. The interferences listed in Table 1 were large enough that the initial stress-free mesh required a significant amount of mesh overlay at the pin-shoulder/box interface. The contact and solution algorithms of JAC2D had difficulty pushing back the overlapping meshes and converging on a solution. This was further complicated by the fact that in some cases the pin and box sections exhibited a slight amount of yielding on preload, making joint preload a nonlinear event. To circumvent these difficulties, a section of material was added to the box section which is identical to the box material except that it has an axial thermal expansion coefficient (see Figure 5). Preload was obtained by heating the model so that this section of material expanded, producing the required amount of displacement to preload the joint.

2.3 Materials and Load History

Since the API specifies allowable stress ranges for sucker rods based on the grade of steel used, the load history is coupled to the material selection. The API specifies many grades of steels for use in sucker rods and box couplings, depending on the particular application and load history. An API Grade C carbon steel was selected as the subject for this study. The API Grade C specification includes any steel with a minimum yield strength of 60 ksi, and a minimum tensile strength of 90 ksi. Hence, these inelastic properties were used in the present

Table 1: API Sucker Rod Joint Make-up Recommendations

Rod Size (in)	Pin Shoulder OD (in)	Minimum Circumferential Displacement (in)	Calculated axial displacement or interference (in)
3/4	1.500	7/32	4.64×10^{-3}
7/8	1.625	9/32	5.51×10^{-3}
1	2.000	12/32	5.97×10^{-3}

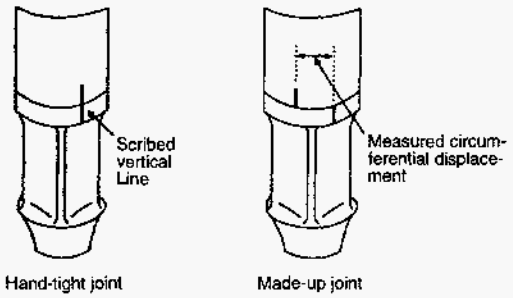

study. The post yield behavior was modeled with a linear hardening modulus of 100 ksi. In addition, an elastic modulus of 29×10^6 psi and a Poisson's ratio of 0.3 were used.

The fatigue limits of API Grade C sucker rods were determined specifically from the modified Goodman plot shown in Figure 7. This diagram shows the allowable stress range for API Grade C steel and identifies three load scenarios selected for analysis in the present study: cycling between -2 ksi and 8 ksi, between 2 ksi and 23 ksi, and between 15 ksi and 30 ksi. In the presentation of the analysis results these load cycles are identified as Cycles 1, 2, and 3, respectively. The three load cycles identified in the modified Goodman diagram (Figure 7) are load cycles which will provide an indefinite service life with respect to rod failure. In addition to the above load cycles, extreme loads of -5 ksi and 40 ksi were chosen for analysis to determine if the threaded coupling behaves elastically under these allowable extreme loads. Assuming that the coupling deformations are linearly elastic while cycling between the extreme loads, then all three load cycles can be studied from a single calculation following this load path. Hence, following preload, all of the models were first subjected to the maximum compressive load (-5 ksi) followed the maximum tensile load (40 ksi). If the coupling were to experience inelastic deformation during this first load cycle (e.g. in the threads), then the coupling stresses would not follow the same path in subsequent load cycles. To determine if this was the case, the models were subjected to an additional load cycle

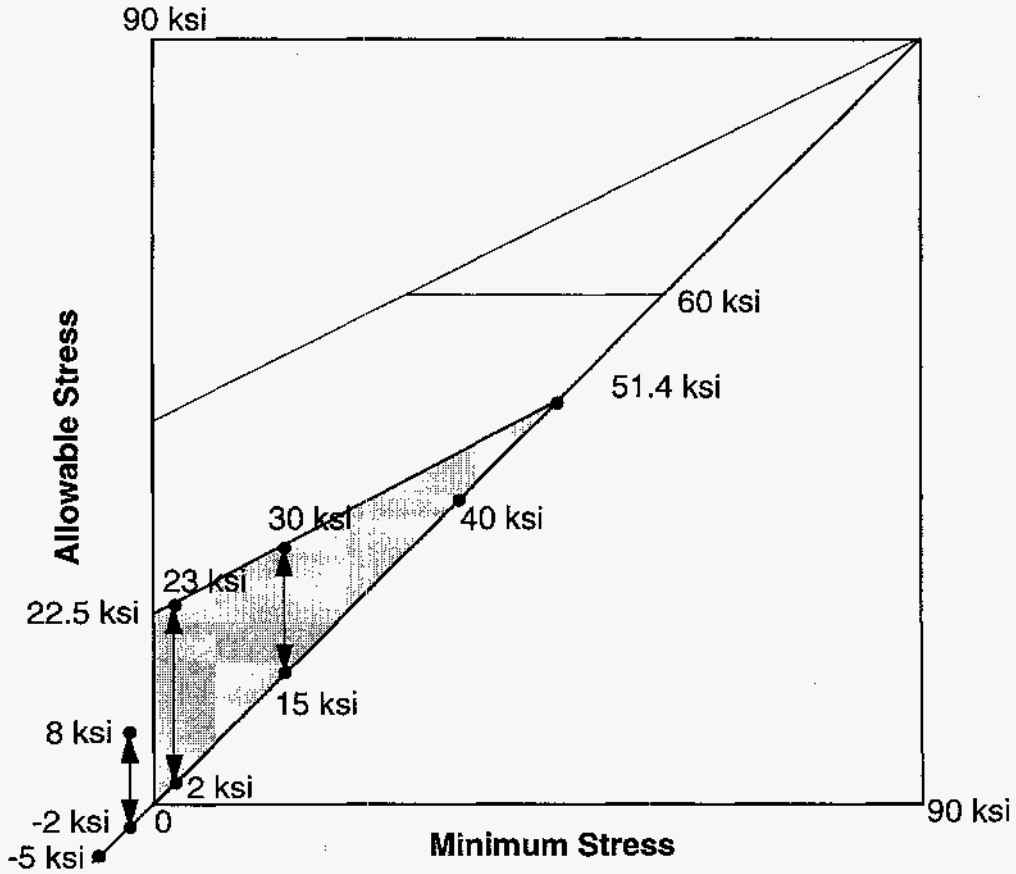

Figure 7. Modified Goodman diagram for API Grade C carbon steel, identifying load cycles and extreme loads selected for analysis.

between the extremes to assure that the stress path was repeated for every point in the coupling.

2.4 Summary of Analysis Cases

A variety of geometries and preloading options have been presented. The particular cases selected for analysis are listed in Table 2. To simplify the presentation of the analysis results, the abbreviation FB is used to identify a coupling with the Flexbar modified pin, SH to identify a slimhole coupling, and SL to identify a coupling with Spiralock threads. In addition, the 3/4, 7/8 and 1-inch coupling sizes are identified as S6, S7, and S8, respectively. The

Table 2: Summary of Analysis Cases

Analysis No	*Coupling Size**	*Rod Size*	*Pin***	*Box****	*Make-Up*
1	F	7/8"	API	API	1.0
2	F	7/8"	API	API	1.5
3	F	7/8"	API	API	0.0
4	F	7/8"	FB	API	1.0
5	SH	7/8"	API	API	1.0
6	SH	7/8"	FB	API	1.0
7	F	3/4"	API	API	1.0
8	F	1"	API	API	1.0
9	F	7/8"	FB	SL	1.0
10	SH	7/8"	API	SL	1.0
11	F	7/8"	API	SL	0.0
12	F	7/8"	API	SL	1.0
13	F	7/8"	API	SL	1.5
14	F	7/8"	API	SL	2.0
15	F	7/8"	API	SL	2.5
16	F	7/8"	API	SL	3.0

* F = full bore, SH = slimhole
** API indicates standard API threads, FB indicates Flexbar extended pin with shoulder
*** SL = Spiralock threads in box section

standard 7/8-inch sucker rod coupling (Analysis 1) was selected as the base case by which to benchmark the other cases. A make-up of 1.0 indicates that the joint is made-up according to the API recommendations. Analyses 2 and 3 are of the same geometry but with make-ups of 1.5 and 0, respectively. A make-up of 1.5 indicates that the joint is made-up to one and a half times the recommended circumferential displacement. Analysis 4 adds the Flexbar pin to this base geometry, while Analysis 5 looks at the slimhole configuration of the base case. Analysis

6 combines both the Flexbar pin and the slimhole box section into a single analysis. Analyses 7 and 8 look at the 3/4 inch and 1 inch versions of the same base coupling. Analysis 9 takes a look at the base coupling geometry with the addition of the Flexbar pin and Spiralock thread modifications. Analysis 10 examines the slimhole version of the base geometry with Spiralock threads. Finally, Analyses 11 through 16 are of the same geometry (base 7/8 inch coupling with Spiralock threads), but with make-ups varying from 0.0 to 3.0.

3 Analysis Results

The purpose of preloading a threaded coupling is to (1) lock the threaded coupling together so that it will not loosen and eventually uncouple, and (2) improve the fatigue resistance of the threaded connection by reducing the stress amplitude in the threaded coupling when subjected to cyclic loading. Hence, the "relative goodness" of the various coupling geometries and preloads analyzed here will be based on how well they accomplish these two objectives.

3.1 Yielding in the Sucker Rod Coupling

If the coupling yields at the same location on every cycle, a condition known as plastic ratcheting, then it will fail in a relatively small number of cycles. Even if the coupling only yields on the first cycle, this will reduce the preload in the coupling. If the preload is reduced enough to cause separation of the coupling, then the coupling integrity and the fatigue life can be compromised.

Figure 8 is a plot of the von Mises distribution in the 7/8-inch API standard coupling at preload (no axial load), maximum compression (-5 ksi), and maximum tension (40 ksi). Recall that the yield strength of the API Grade C steel is 60 ksi. Hence, a red contour is indicative of regions which have yielded. As the figure shows, during preload the steel yields in the pin shoulder, the pin neck, and at the root of the first three pin threads. Yielding during preload was predicted in all of the simulations except for those which had a zero makeup. When subjected to the maximum compressive load, the pin shoulder yields further while no further yielding is experienced in the threads. Finally, when subjected to the maximum tensile load, the pin threads and pin neck yield even more while no further yielding is experienced in the pin shoulder. Yielding during the first load cycle was predicted in all of the simulations. However, none of the simulations experienced further yielding on the second load cycle.

The von Mises stress distributions in all of the simulated couplings using the API thread form are very similar to that shown in Figure 8. Only the Spiralock modification produced a significant change in the coupling mechanics. Figure 9 is a plot of the von Mises distribution in the 7/8-inch Spiralock coupling (Analysis 12) at preload (no axial load), maximum compression (-5 ksi), and maximum tension (40 ksi). The major difference between the Spiralock and API simulations is that the stresses in the pin and box bodies are much smaller in the Spiralock case than in the API case, indicating that the Spiralock coupling is not generating as much preload. This will be better quantified in the following section. During the make-up process the Spiralock coupling yields only at the tips of the pin threads. This differs from the API coupling which yielded in the threads, the pin neck, and the pin shoulder. The reason for the thread yielding is the very localized point contact between the pin and box threads. This point contact generates very high deviatoric stresses in the pin threads upon

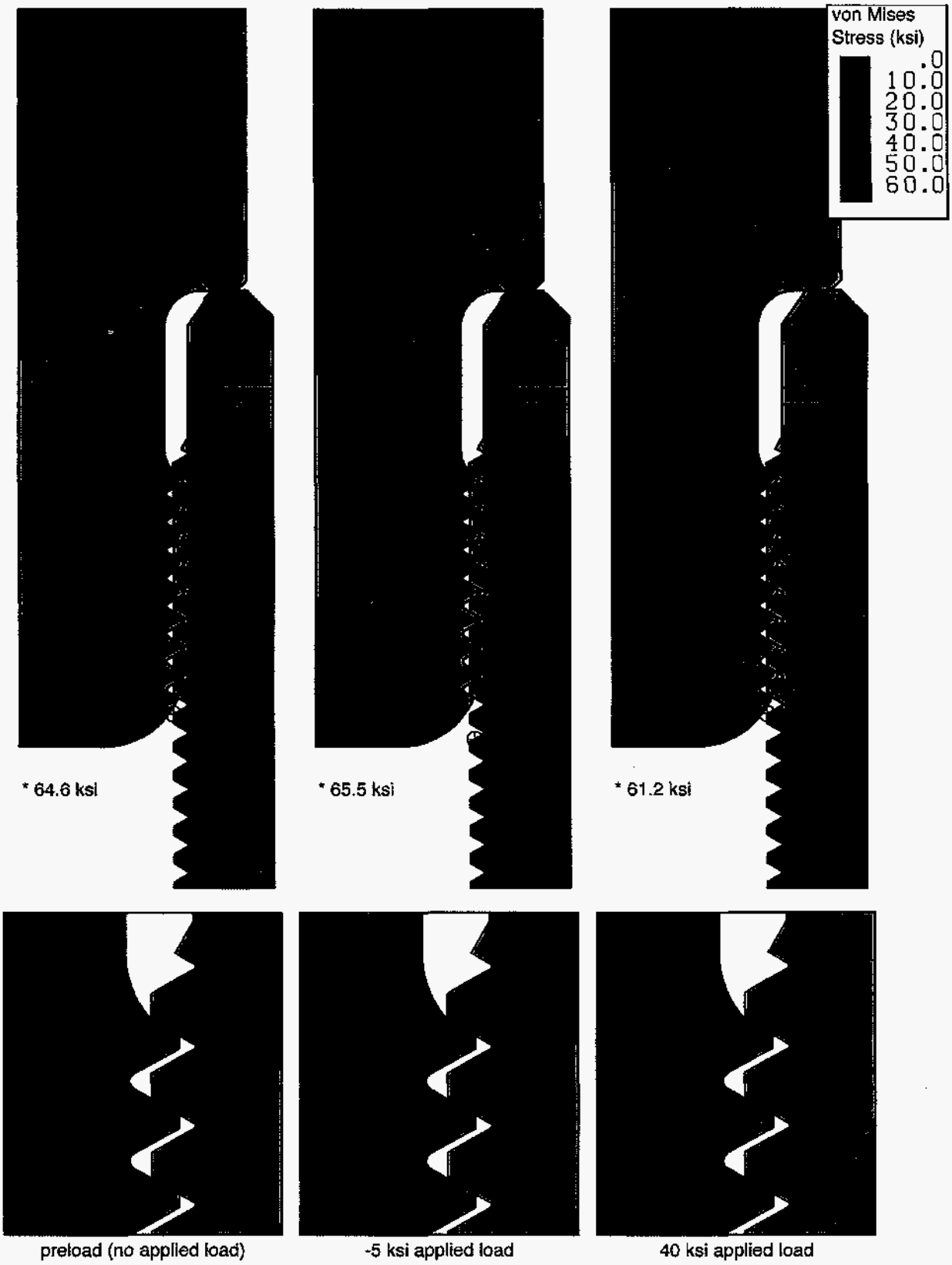

Figure 8. Von Mises stress distribution (ksi) in the 7/8-inch API standard coupling (Analysis 1) at preload, maximum compression, and maximum tensile loads.

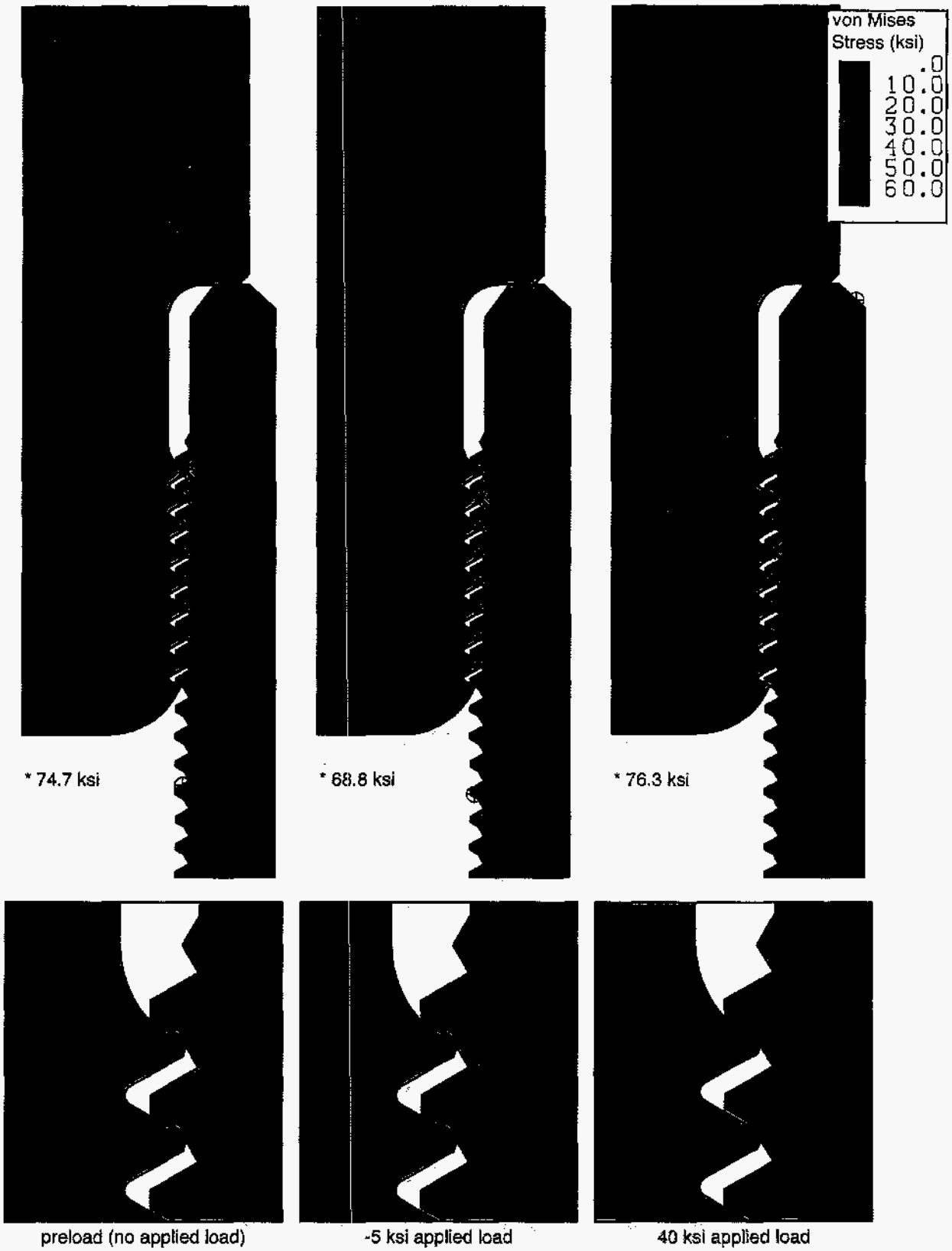

Figure 9. Von Mises stress distribution (ksi) in the 7/8-inch Spiralock coupling (Analysis 12) at preload, maximum compression, and maximum tensile loads.

loading. The deformation of the pin thread tips is so great that it reduces the preload in the coupling. No further yielding occurs when the coupling is subjected to the maximum compressive load. This is indicated by the fact that the maximum yield stress at the maximum compressive load (68.8 ksi) is less than that at preload (74.7 ksi). Finally, when subjected to the maximum tensile load, the pin threads yield even more, conforming to the shape of the box threads. No further yielding was predicted to occur in the second load cycle. Although the yield regions in the above examples appear to be small, these nonlinear deformations have a profound effect on the performance of the couplings as will be observed in the following section.

3.2 Load Distribution in Threaded Coupling During Load Cycling

The sucker rod coupling joint is basically a bolted joint in tension. A better understanding of the numerical results presented in this report is facilitated by a review the theory of bolted joints [3]. The illustration in Figure 10 defines many of the terms used in this discussion.

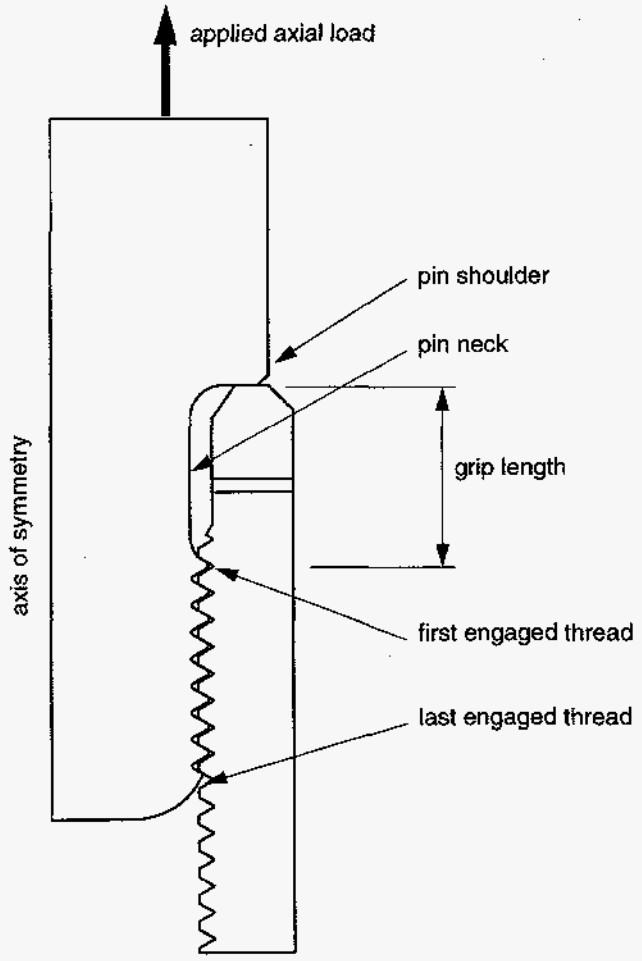

Figure 10. Illustration of sucker rod coupling.

Treating both the pin and the box sections as elastic members, the deflection (δ) of each under simple tension or compression can be expressed as

$$\delta = \frac{Fl}{AE} \tag{2}$$

where F is force, A is the cross-sectional area of the pin or box section, E is the modulus of elasticity, and l is the grip length. As shown in Figure 10, the grip length is assumed to extend from the pin shoulder (where it contacts the box) to a distance just below the first engaged threads. The actual grip length, though difficult to calculate, is slightly longer. The threads can be neglected when calculating the cross-sectional areas of the pin and box sections since, in most cases, the majority of the grip length is not threaded (see Figure 6). Therefore, the stiffness constant of each can be expressed as:

$$k = \frac{F}{\delta} = \frac{AE}{l} \tag{3}$$

Note that the bolt theory presented below is primarily concerned with the material between the pin shoulder and the first engaged thread. It is this material which carries and benefits from the initial preload F_i.

When an external load P is applied to the preloaded sucker-rod coupling, there is a change in the deformation of the pin and the box sections. The pin, initially in tension, gets longer. This increase in deformation of the pin is

$$\Delta\delta_p = \frac{P_p}{k_p} \tag{4}$$

where the subscript p denotes the pin, and P_p is the portion of the load P taken by the pin. The box section is initially in compression due to the preload. When the external load is applied, this compression will decrease. The decrease in the deformation of the box section is

$$\Delta\delta_b = \frac{P_b}{k_b} \tag{5}$$

where P_b is the portion of the load P taken by the box section. If the pin and box section have not separated, the increase in deformation of the pin must equal the decrease in deformation of the box.

$$\frac{P_p}{k_p} = \frac{P_b}{k_b} \tag{6}$$

Since $P = P_b + P_p$

$$P_p = \frac{k_p P}{k_p + k_b} \tag{7}$$

Given an initial preload of F_i, the resultant load on the pin is

$$F_p = P_p + F_i = \frac{k_p P}{k_p + k_b} + F_i = \gamma_p P + F_i \tag{8}$$

Similarly, the resultant load in the box is

$$F_b = \frac{k_b P}{k_p + k_b} - F_i = \gamma_b P - F_i \tag{9}$$

where γ_p and γ_b are load partitioning factors. The load partitioning factors are the fractions of the applied load which are taken by each member.

$$\gamma_p = \frac{k_p}{k_p + k_b} = \gamma_b - 1 \tag{10}$$

Equations 2 thru 10 apply as long as there is compression between the pin and box sections. If the external load is large enough to remove this compression completely, the pin and box will separate and the entire load will be carried by the pin.

$$F_p = P \quad \text{(after separation)} \tag{11}$$

This review of threaded connection theory is particularly insightful into the design of couplings subjected to cyclic load conditions. Under cyclic loading conditions the pin is more likely to fail due to fatigue since crack growth only occurs under tensile stress conditions. Prior to separation, the resultant load in the pin (F_p) varies according to Equation (8) which, assuming a finite box stiffness, has a slope (γ_p) of less than one with respect to the external varying load. Once separation has occurred, the slope of F_p increases to one (Equation 11). This tells us two things. First, to improve the fatigue resistance of a sucker rod coupling, the joint should have a preload sufficiently high to prevent separation of the pin and box. Second, the amplitude of the tensile load cycle in the pin section can be reduced by increasing the stiffness of the box section relative to the pin. By doing this, the pin load partitioning factor (γ_p) is reduced. Although the box load partitioning factor (γ_b) is increased, this is not significant since the resultant load in the box section is cycling in compression.

It is difficult to exactly determine the stiffness of the pin and box sections. However, since the length and elastic modulus are the same in both the box and pin, the relative stiffness of the two components should be proportional to their cross-sectional areas. Hence,

$$\gamma_p \approx \frac{A_p}{A_p + A_b} \tag{12}$$

Table 3 shows the calculated cross-sectional areas and approximate load partitioning factors for the various geometries evaluated in this study. All three coupling sizes (for 3/4, 7/8 and 1-inch rods) have similar load partitioning factors, transferring approximately 35 percent of the applied load to the pin. The amount of load taken by the pin increases to nearly 48 percent for the slimhole configuration due to the smaller cross-sectional area of the slimhole box section.

Figures 11 thru 14 show the pin load and the coupling force as a function of the applied rod load for all 16 calculations performed for this study. Each case will be discussed in greater detail after some general comments. Each plot identifies the three different load cycles under investigation: Cycle 1 (-2 ksi to 8 ksi), Cycle 2 (2 ksi to 23 ksi), and Cycle 3 (15 ksi to 30 ksi). The pin load is the total axial force in the neck of the pin (the region between the pin shoulder and the threaded section of the pin). This was calculated by integrating the axial force (on a per element basis) across the cross-sectional area of the neck. The coupling force is the total axial load at the interface of the pin shoulder and box section. This was calculated by integrating the axial force in the axially expanding section of the box coupling (see Figure 5) over the cross-sectional area of the coupling at this location. For both calculated quantities a positive load is tensile while a negative load is compressive.

Since the axial load history was specified in the simulations as a pressure boundary condition and is the same for all of the simulations, it is also presented in the plots in pressure units to permit direct comparison of the many simulations (i.e. the different rod sizes result in different axial force quantities). All of the load diagrams follow the history of the simulations which initiated at preload with no axial load. Next, they were loaded to the maximum compressive load of -5 ksi, and then loaded in tension up to the maximum tensile load of 40 ksi. This load sequence is represented as a dashed line in the plots. An additional load cycle to -5 ksi and again to 40 ksi was simulated to determine if the coupling stress response follows the same path, assuring that the deformations are linear elastic. This second load cycle is represented in the plots as a solid line. The data points on the plots indicate points at which the finite element solutions were reported and are of no other significance. Because the couplings exhibit some yielding on the first application of compression and tension loads, the dashed line (representing the first load cycle) and the solid line (representing the second load cycle) do not overlap in any of the simulations. However, the compression stroke (40 ksi to -5 ksi) and the tension stroke (-5 ksi to 40 ksi) of the second load cycle follow the exact same path for

Table 3: Pin and Box Cross-Sectional Areas and Load Partitioning Factors for Various Coupling Geometries

Geometry	Pin Area, A_p (in^2)	Box Area, A_b (in^2)	γ_p	γ_b
S6	0.6576	1.158	0.362	0.638
S7	0.8495	1.440	0.371	0.629
S8	1.1820	2.234	0.346	0.654
S7, SH	0.8495	0.9335	0.476	0.524

each of the simulations, indicating that the second load cycle is elastic throughout the entire load range.

By looking at both the pin load and coupling force for each configuration, it is easier to identify where the applied axial load is transferred. As was shown in the discussion on threaded couplings, the applied load is carried by the pin and the box sections. The portion of the load carried by the pin is the difference between the pin load at load and the pinload at preload. Similarly, the portion of load carried by the box section is the difference between the coupling force at load and the coupling force at preload. The sum of these two loads is always equal to the total load applied to the sucker rod.

The most significant performance characteristics identified in these plots are summarized in Table 4. This table includes the initial preload before the coupling is subjected to any loading, and the preload after the coupling has been cycled between the maximum and minimum loads. The former is the preload right after make-up, while the latter accounts for any loss in preload due to yielding in the first load cycle. The last column in Table 4 is the pin load partitioning factor for each of the simulations. This was calculated by taking the difference between the pin load at the maximum applied tensile load (40 ksi) and the pin load at zero applied load (preload after load cycling), and dividing by the total applied load (40 ksi times the rod area). The results summarized in Table 4 are helpful in the following more thorough discussion of each case.

Figure 11 shows the load plots for the 3/4, 7/8, and 1-inch coupling sizes. Note that for all three sizes, the pin load and coupling force do not return to the same exact value after the coupling is initially subjected to the maximum compression load and then returned to zero applied load. This occurs because the pin shoulder yields during the first compression cycle (as shown in Figure 8). After the coupling is subjected to the maximum tensile load and returned to zero, the preload changes once again. This time the change is due to the yielding in the pin threads predicted on the first application of the maximum tensile load (as shown in Figure 8). After the initial yielding in the first tension and compression cycles, the coupling behaves elastically throughout the entire load range, as evidenced by the linear relationship of pin load and coupling force with respect to axial load. The coupling force remains compressive throughout the load range, indicating that none of the coupling sizes separate. Recall that the portion of load carried by the pin is equal to the change in pin load from preload to the loaded condition. At the maximum applied load of 40 ksi, the load in the 7/8-inch rod is approximately 50 ksi, while at preload the pin load is approximately 40 ksi. Hence, the pin takes 9.7 kip of the 24 kip applied load, resulting in a load partitioning factor of 0.402. The load partitioning factors for the S6 and S8 rods are 0.373 and 0.344, respectively. In a relative sense, the numerically calculated load partitioning factors compare very well with the theoretical values reported in Table 3. The partitioning factor for the 7/8-inch coupling (S7) is the largest, while that of the 1-inch coupling (S8) is the smallest.

Figure 12 shows the load plots for the base geometry (S7) with make-ups of 0.0, 1.0, and 1.5. As the plots show, the additional 50 percent of make-up produces very little additional preload in the coupling. This is due to the fact that the pin shoulder of the S7 coupling yields during the make-up process. Additional make-up produces further yielding of the shoulder, but very little additional preload. As expected, the 0.0 make-up case separates immediately upon

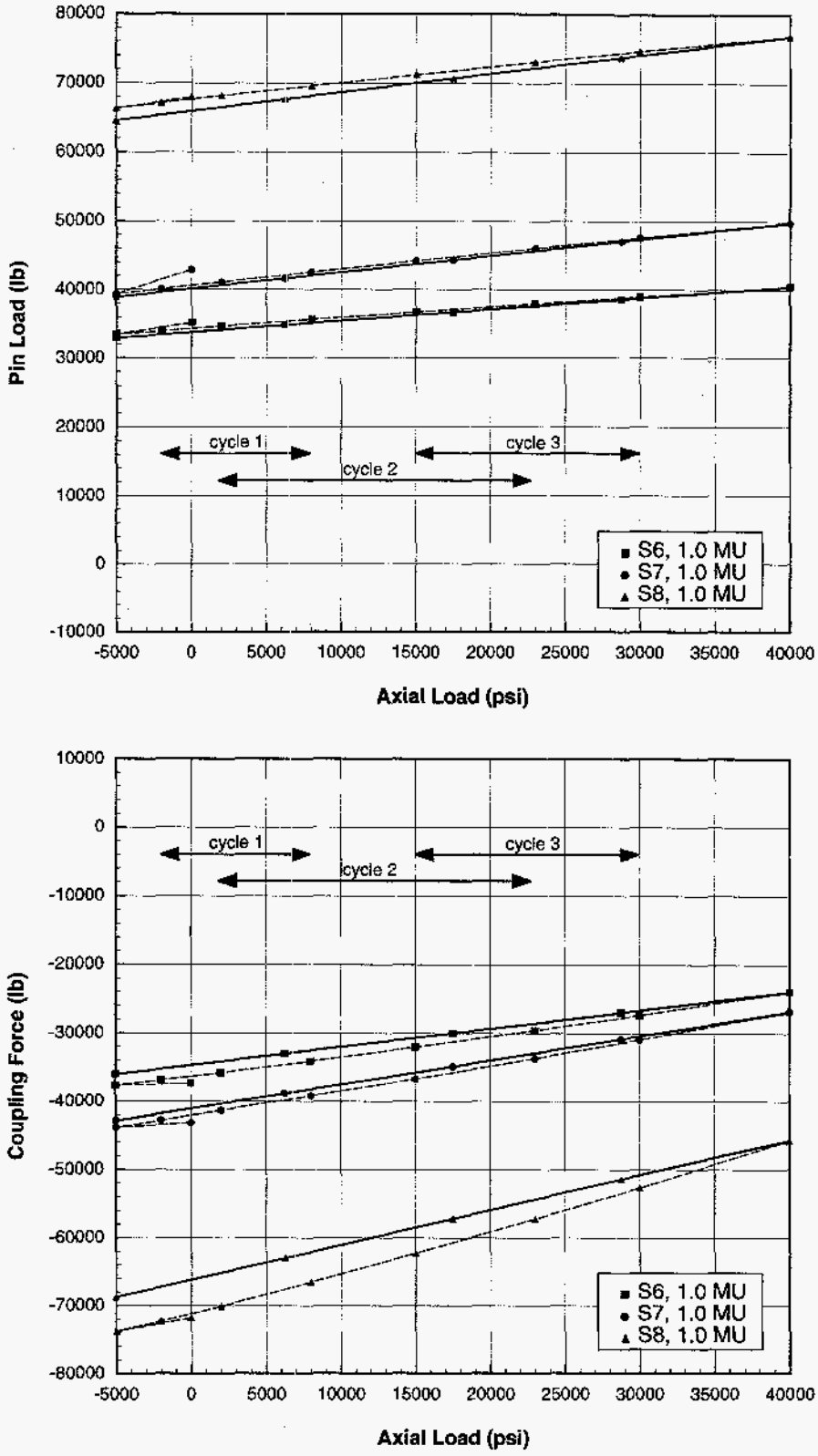

Figure 11. Pin load and coupling force as a function of axial load for the 3/4, 7/8, and 1-inch coupling sizes (S6, S7, and S8, respectively).

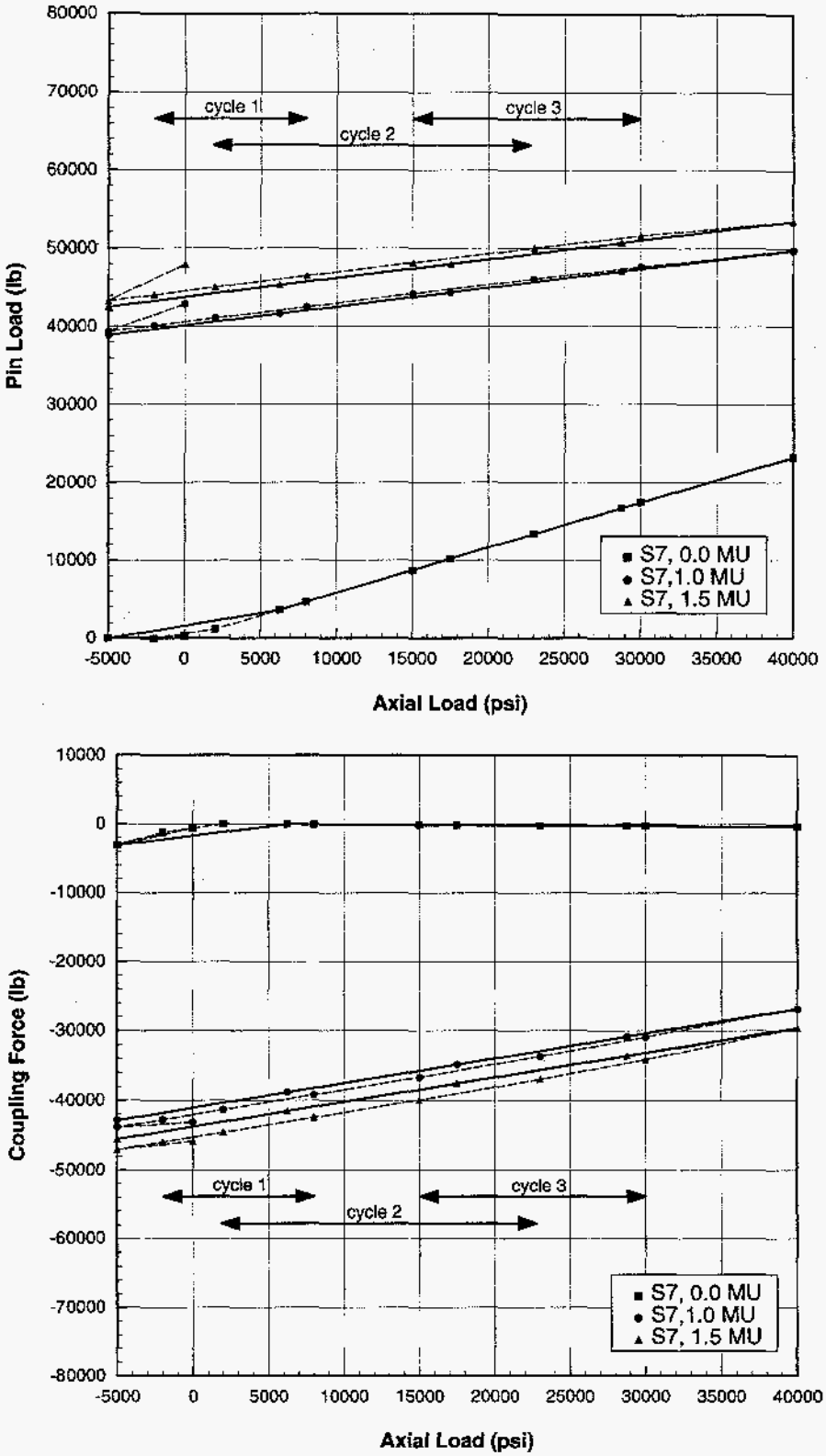

Figure 12. Pin load and coupling force as a function of axial load for the 7/8-inch standard API coupling size (S7) with make-ups of 0.0, 1.0, and 1.5.

tensile loading. At the maximum axial load, the pin is carrying the entire 24.1 kip load. The slope of the pin load diagram for the 0.0 make-up simulation is greater than that of the preloaded cases. Hence, for any of the three load cycles labeled in the plot the stress amplitude will be approximately 2.7 times larger ($1/\gamma_p$) in the pin with no preload.

Figure 13 shows the load plots for various combinations of the Flexbar (FB), Spiralock (SL), and slimhole (SH) geometry modifications to the base geometry (S7). The Flexbar modification to the base coupling geometry (S7) produces very little change in the preload at full make-up, reducing from 40.1 kip to 38.4 kip. This was expected since the Flexbar modification merely increases the grip length of the coupling but does not change the cross-sectional areas (i.e. the stiffness) of the pin and box sections. Hence, the performance of the Flexbar coupling is nearly identical, in terms of load partitioning, to that of the base API geometry. The slimhole variation of the base geometry reduces the preload to 36.0 kip. Because the slimhole modification reduces the cross-sectional area of the box section, the relative stiffness of the pin and box are changed. This is evidenced in slope changes in both the pin load and coupling force plots. At the maximum load, the slimhole pin takes approximately 11 kip of the 24 kip applied axial load, resulting in a pin load partition of 0.456. This relative increase in the predicted partitioning factor agrees well with the theoretical partitioning factor for the slimhole geometry (Table 3).

As seen in Figure 13, the inclusion of the Spiralock thread form to the base geometry produces a significant reduction in the preload of the fully made-up joint, reducing from 42 kip to 26 kip. This reduction in the preload is due to a greater amount of yielding of the Spiralock threads relative to the standard API threads. Because the preload is reduced, the coupling separates at approximately 30 ksi of axial load. The separation is evidenced by the fact that the coupling force goes to zero, while the slope of the pin load plot increases (indicating that the pin is carrying all of the load). The increased load on the pin causes the threads to yield even further. As stated in the previous section, yielding of the pin threads and shoulder reduces the preload in the coupling. Note that when the load applied to the Spiralock coupling is returned to zero, the preload is reduced from 15.3 kip to 1.8 kip. The effects of adding the slimhole or Flexbar modifications to the Spiralock threads is minimal. The performance with these additional modifications is nearly identical to the base Spiralock geometry. These results suggest that the Spiralock thread form requires a greater make-up than a standard API coupling to achieve the same amount of preload. Figure 14 shows the load plots for the Spiralock coupling (SL) with make-ups of 0.0, 1.0,1.5, 2.0, 2.5, and 3.0. The Spiralock coupling separates with make-ups of 0.0 and 1.0. Once separation occurs, the pin carries the entire axial load (a maximum 24.1 kip). The 1.5 make-up case experiences a greater amount of thread yielding during the make-up process. As a result, the coupling does not separate and a significant amount of the preload is retained after the initial compression and tension loads (reducing from 20.7 kip to 20.5 kip). While a make-up of 1.5 is sufficient to prevent separation within the load range, a make-up of over 2.0 is required to obtain the same amount of preload as the fully made-up 7/8-inch API coupling. Further increases in the make-up over 2.0 produce very small increases in the preload. As in the case of the base geometry (see Figure 12), this is due to yielding of the pin shoulder during preload.

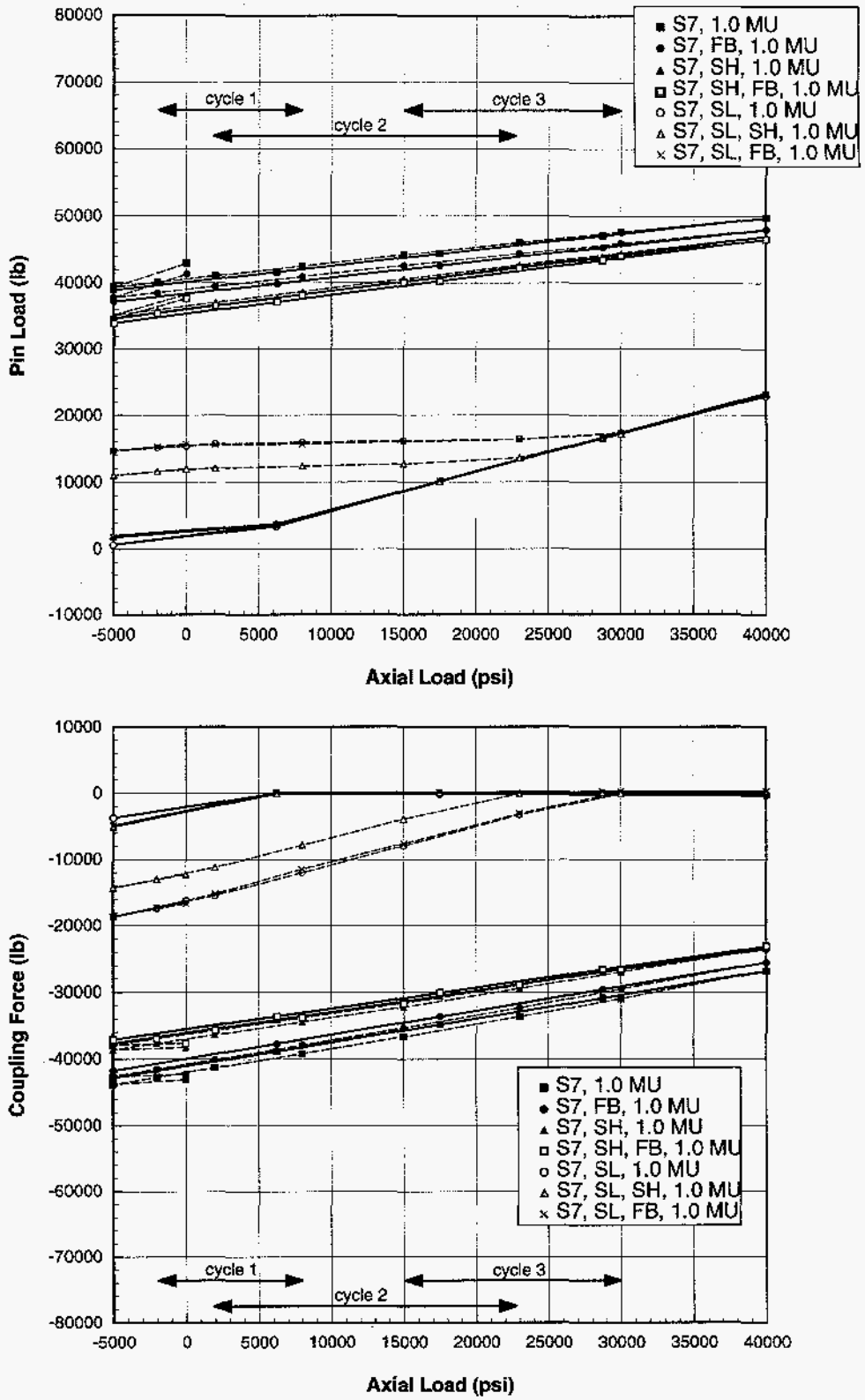

Figure 13. Pin load and coupling force as a function of axial load for various combinations of the Flexbar (FB), Spiralock (SL), and slimhole (SH) geometry modifications to the base geometry (S7).

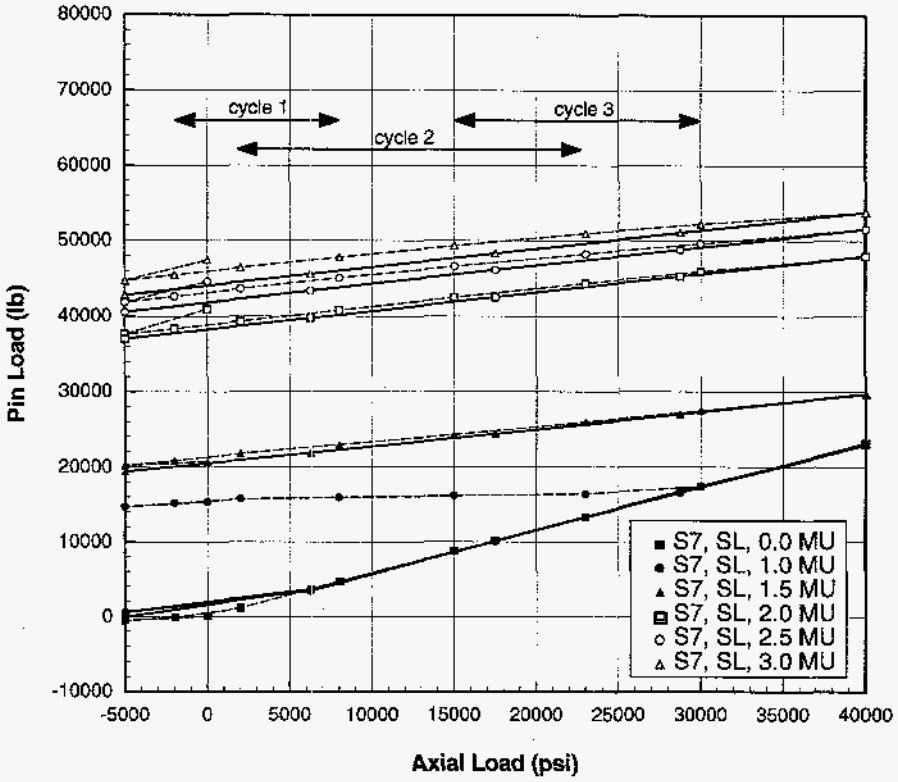

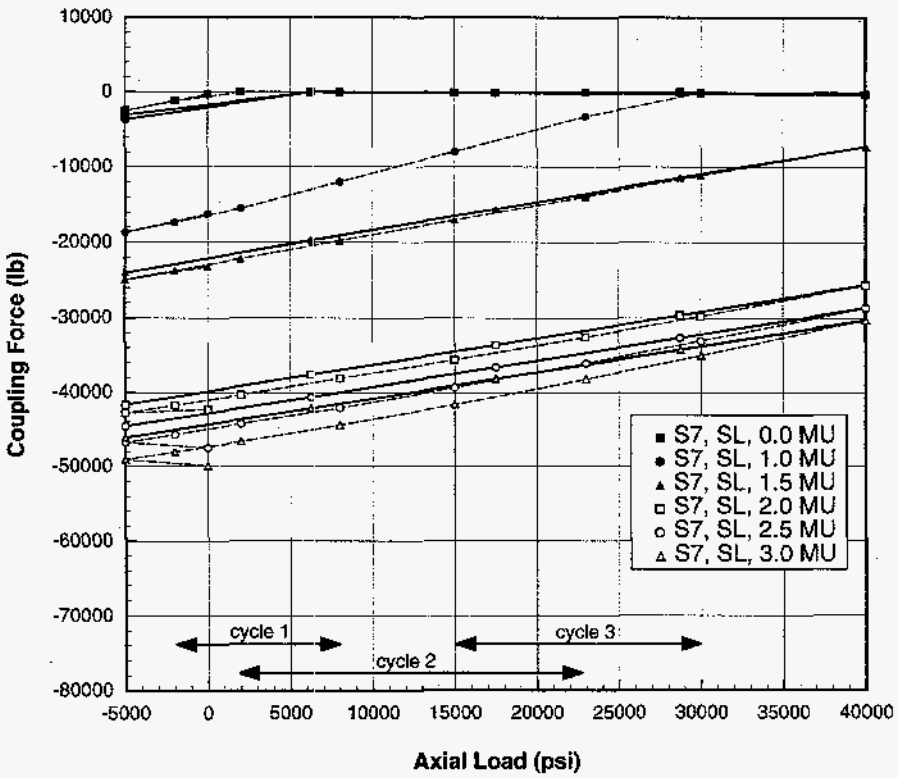

Figure 14. Pin load and coupling force as a function of axial load for the base geometry (S7) with Spiralock threads (SL) and make-ups of 0.0, 1.0,1.5, 2.0, 2.5, and 3.0.

Table 4: Summary of Coupling Performance for Various Analysis Cases

Analysis No	Description*	Initial Preload		Preload after Load Cycle		Load Partitioning Factor at Max Tensile Load**
		Load (kip)	Avg Stress (ksi)	Load (kip)	Avg Stress (ksi)	
1	S7, 1.0 MU	42.9	50.5	40.1	47.2	0.402
2	S7, 1.5 MU	47.9	56.4	43.8	51.6	0.398
3	S7, 0.0 MU	0.0	0.0	0.0	0.0	1.0
4	S7, FB, 1.0 MU	41.3	48.6	38.4	45.2	0.398
5	S7, SH, 1.0 MU	38.2	45.0	36.0	42.4	0.456
6	S7, SH, FB, 1.0 MU	41.3	48.6	35.3	41.6	0.469
7	S6, 1.0 MU	35.1	53.4	33.8	51.4	0.373
8	S8, 1.0 MU	67.9	57.4	66.0	55.8	0.344
9	S7, FB, SL, 1.0 MU	15.7	18.5	2.6	3.06	1.0
10	S7, SL, SH, 1.0 MU	11.9	14.0	2.8	3.30	1.0
11	S7, SL, 0.0 MU	0.0	0.0	0.0	0.0	1.0
12	S7, SL, 1.0 MU	15.3	18.0	1.8	2.12	1.0
13	S7, SL, 1.5 MU	20.7	24.4	20.5	24.1	0.382
14	S7, SL, 2.0 MU	41.0	48.3	38.2	45.0	0.407
15	S7, SL, 2.5 MU	44.3	52.1	41.8	49.2	0.402
16	S7, SL, 3.0 MU	47.4	55.8	44.0	51.8	0.407

* SH = slimhole, FB = Flexbar, SL = Spiralock
** Maximum load of 40 ksi is 17.7 kip for S6, 24.1 kip for S7, and 31.4 kip for S8

3.3 Estimating Fatigue Life of Sucker Rod Couplings

In the previous section, the load distribution in the threaded coupling was discussed in detail. The factors that affect the stress amplitude in the pin under cyclic loading conditions were examined. It was mentioned that the fatigue resistance of the coupling would be greatly improved if the stress amplitude in the pin were minimized. However, this discussion was presented in terms of loads and nominal stresses. These nominal stresses can be greatly affected by the geometrical features of the coupling, producing stress risers in the coupling which will provide preferred sites for crack initiation and growth. In this section, the stress risers will be identified and the fatigue response at these locations will be characterized for each of the simulations performed for this study in an attempt to identify features which could limit the service life of the coupling.

3.3.1 Considerations in Life Prediction

Life prediction involves calculating the stresses in the component based on the given material, component geometry, and applied loads. Through the application of an empirical failure criterion, the calculated stresses are then transformed into fatigue damage or crack growth. The following section describes the failure criterion used in the present study.

In metals such as steel, fatigue damage and crack growth occurs by a process called reversed-slip [4]. Slip is the process by which planes of atoms move past each other along a slip plane. The amount of slip on a given cycle relates to the amount of cyclic stress imposed. The slip process is responsible for fatigue crack initiation and crack growth processes. The differences in the slip behavior during crack initiation and growth are in the magnitude of the slip and the volume of the material affected. Slip during crack initiation is low level but widespread compared to crack growth. During crack growth, the magnitude of slip is relatively large and concentrated at the small plastic zone at the crack tip. Hence, during crack initiation, slip is concentrated in highly stressed regions. Once cracking begins, the deformation, formerly accommodated by slip in the highly stressed regions, is taken up by deformation in the region surrounding the crack tip. Slip occurs easiest at the surface and is concentrated by material and geometric stress risers [4]. This is why most fatigue failures initiate at the surface of the component. Hence, the fatigue life is affected by processing and other factors, such as corrosion, which alter the surface and create stress risers.

The fatigue process occurs everywhere in a structural component where the stresses are large enough to cause continued reversed-slip. Since the rate of the fatigue process is proportional to the magnitude of the reversed-slip, the fatigue process is problematic in regions where the stresses are the largest. These regions typically correspond to stress risers and are critical in the fatigue life of the component. The fatigue process includes a period of damage accumulation leading to *crack initiation* and a period of *crack growth*, ultimately ending with the catastrophic failure of the component. Hence, the total life of the component is the sum of the crack initiation and propagation lives.

The methods used in estimating the crack initiation and propagation lives are fundamentally different since the presence of a crack alters the stress field of a component. The finite element method is based on a continuum formulation and does not accurately calculate the stress field ahead of crack tips unless specialized elements are used. Hence the stresses calculated using this technology are due to the component geometry as modeled. Until a crack forms which is long enough to disturb the stress field, an approach based on these calculated stresses can be used to simulate the damage accumulation process. Such an approach for life prediction is based on fatigue data developed from unnotched specimens. Once a crack forms which is long enough to disturb the stress field, the slip process concentrates at the crack tip. Stresses located even a small distance from the crack (i.e. those determined from a finite element simulation) no longer characterize the magnitude of slip at the crack tip. Hence, nominal stresses cannot be used to characterize the slip process at the crack tip. Methods of lifetime estimation which account for the crack's effect on the stress field involve the use of fracture mechanics [5]. These approaches to life prediction relate the calculated stress field to a crack growth rate and are based on fatigue data developed from notched or precracked specimens.

The manufacturers and designers of sucker rod systems exercise extreme care in controlling the factors which affect the fatigue life of sucker rods. The rods are polished, the specified load range accounts for corrosion, and the thread geometry is designed to minimize stress risers by rounding the root of the threads. As an indication of design intent, sucker rods are sized based on a modified Goodman criteria which ensures an indefinite fatigue life. Hence, this study has taken a conservative approach to lifetime estimation by choosing to apply only crack initiation methods to the life estimation of sucker rod couplings. This study neglects the crack growth life which can contribute a significant number of cycles to the component life. Instead, this study assumes that the coupling has failed once fatigue damage has produced a crack.

As previously stated, crack initiation methods are based on fatigue data developed from unnotched specimens. In these tests, a specimen is subjected to alternating stresses that vary between fixed limits of maximum and minimum stress until failure occurs. The load range is typically characterized by a stress ratio, defined as follows:

$$R = \frac{\sigma_{min}}{\sigma_{max}} \tag{13}$$

Alternatively, the load range is sometimes described in terms of a mean stress and an alternating stress, defined as follows:

$$\sigma_m = \frac{\sigma_{max} + \sigma_{min}}{2} \tag{14}$$

$$\sigma_a = \frac{\sigma_{max} - \sigma_{min}}{2} \tag{15}$$

Fatigue tests are repeated for other specimens at the same stress ratio but different stress amplitudes. The results of these tests are plotted to form an *S-N* diagram. A family of *S-N* curves for a material tested at various stress ratios is shown schematically in Figure 15. In the case of ferrous metals and alloys, the fatigue strength decreases as the number of cycles increases, asymptotically approaching the *fatigue limit* or *endurance limit*. If the stress amplitude in a component does not reach the fatigue limit for a given stress ratio, an infinite number of load cycles can be applied to the component without causing failure. An endurance limit does not exist for nonferrous materials. Because *S-N* curves have this horizontal asymptote, a small change in the stress amplitude can result in a large change in the number of cycles to failure. Figure 15 also illustrates the effect of stress ratio on the fatigue life and endurance limits. For a given lifetime, as the stress ratio increases, the stress amplitude decreases. Similarly, the endurance limit decreases as the stress ratio increases. Hence, the fatigue life of a component is effectively reduced by the presence of a mean stress.

The data from *S-N* curves like that illustrated in Figure 15 can be used to construct a modified Goodman diagram. The modified Goodman diagram illustrated in Figure 3 is constructed from endurance limit data, hence, providing an indefinite fatigue life. However, a modified

Goodman diagram can be constructed for any finite life (e.g. 10^5 cycles). The modified Goodman diagram illustrated in Figure 3 exhibits the same dependence on mean stress as the plot in Figure 15. For example, under complete load reversal (R = -1.0), the allowable stress amplitude is *T/3*. For a fluctuating load (R = 0.0), the allowable stress reduces to *T/4*. The allowable stress amplitude ($\Delta\sigma$) continues to decrease up to the limit where the minimum and maximum stress converge to the ultimate tensile strength of the material. It appears that the allowable stress range adopted by the API (the shaded area in Figure 3) represents a conservative application of the modified Goodman diagram. This conservatism was probably adopted to ensure that the maximum stress always stay below the yield strength of the sucker rod material (approximately 66 percent of the ultimate tensile strength of API Grade C steel).

3.3.2 Fatigue Damage Criterion for Multiaxial Stress

Nearly all fatigue data is based on uniaxial tests. Under uniaxial conditions, the axial stress, von Mises stress, and maximum principal stress are all equal. Furthermore, the load direction in a uniaxial test never changes throughout the test. Hence, uniaxial test data apply directly to components which are similarly loaded. Since sucker rods are loaded uniaxially, their fatigue performance can be determined directly from fatigue data. In cases where the component is subjected to a multiaxial stress state, stress measures such as the von Mises stress and maximum principal stress are not necessarily equal. Hence, an equivalence criteria must be developed to provide a viable basis to relate the multiaxial state of stress being analyzed to the predominantly uniaxial data which exists in the reference data.

There are two cases of multiaxial stress, referred to as simple and complex multiaxial stress. Simple multiaxial stress refers to the case in which the principal alternating stresses do not change their direction relative to the stressed part. Complex multiaxial stress refers to the case

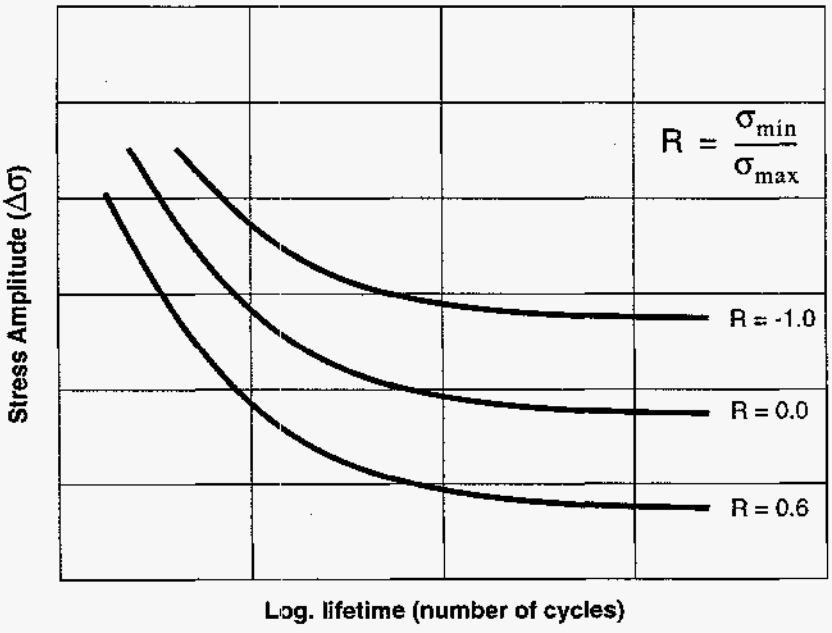

Figure 15. Schematic *S-N* curves for steel at various stress ratios.

in which the directions of the alternating principal stresses change. The first case can be handled easily by calculating the appropriate equivalent stress [7]. The later case is considerably more difficult to analyze and is considered to be beyond the current state of technology [4]. Figure 16 shows the maximum principal stress directions in the threads of the 7/8-inch API coupling at minimum (-5 ksi) and maximum (40 ksi) loads. The vectors show only the direction of the maximum principal stress (i.e. the vector lengths are not proportional to the magnitude of the maximum principal stress). The figure shows that the maximum principal stress directions do not change between these extreme loads. In fact, the maximum principal stress directions do not change for any of the load steps reported by the simulations. Since the calculations are axisymmetric, the hoop direction is one of the principal stresses and its direction never changes. Since the principal stress directions are orthogonal, it reasons that the third principal stress direction does not change either. Hence, sucker rod simulations represent a case of simple multiaxial stress and, as such, can be analyzed with a simple equivalence criteria.

The present study uses Sines' method [7,8,9] to determine an equivalent stress for comparison with test data. Although no test data exists specifically for API Grade C steel, the method will be useful in identifying regions with a high potential for crack initiation and to evaluate the relative effects of various design changes on the coupling fatigue life. The method states that the permissible effective alternating stress is a linear function of the mean hydrostatic stress. This can be mathematically expressed as follows:

$$\sigma_a + k\bar{\sigma}_m \leq A \tag{16}$$

where σ_a is the effective alternating stress,
$\bar{\sigma}_m$ is the mean hydrostatic stress,

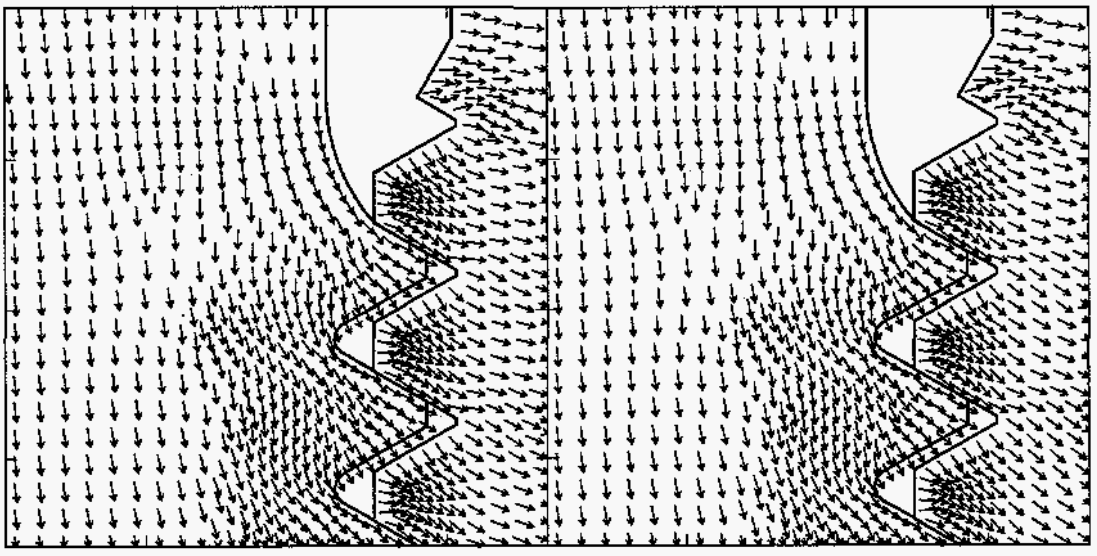

Figure 16. Maximum principal stress directions in the 7/8-inch API standard coupling at minimum (-5 ksi) and maximum (40 ksi) loads.

k is a constant specific to the material and fatigue life, and
A is the assumed failure criteria.

As long as the left side of Equation (16) is less than the right side, the multiaxial stress state will not cause failure of the material within the desired life. The constants k and A change with the assumed fatigue life.

This criterion can be expressed in terms of the principal stresses as follows:

$$\frac{[(S_{a1}-S_{a2})^2+(S_{a2}-S_{a3})^2+(S_{a3}-S_{a1})^2]^{1/2}}{\sqrt{2}} \le S_N - m\frac{(S_{m1}+S_{m2}+S_{m3})}{3} \tag{17}$$

where S_{ai} = alternating component of the principal stresses
S_{mi} = mean component of the principal stress
S_N = uniaxially fully reversed fatigue stress for N cycles
m = coefficient of mean stress influence

It should be noted that S_N is the endurance limit when N approaches infinity. The constants m and S_N which describe the fatigue properties for a material can be determined from two fatigue curves in which the stress ratios are appreciably different. Two curves which are convenient for the determination of these constants are the reversed axial test ($R = -1.0$) and the zero-tension fluctuating stress ($R = 0.0$). In the fully reversed uniaxial test, Equation (17) reduces to:

$$S_{a1} = S_N \tag{18}$$

verifying that S_N is the amplitude of the uniaxial reversed fatigue stress. In the zero-tension fluctuating stress test, the criterion reduces to:

$$f_N = S_N - m\frac{f}{3} \tag{19}$$

where f_N is the amplitude of the fluctuating stress ($R = 0.0$) which would cause failure at the same lifetime as the reversed stress S_N ($R = -1.0$). Solving the above two equations for m yields:

$$m = 3\left(\frac{S_N}{f_N} - 1\right) \tag{20}$$

As previously stated, most fatigue failures initiate at the surface where the stress state is biaxial. In a biaxial stress state, Equation (17) defines lines of constant von Mises stress which form ellipses that enclose regions of "safe" alternating stress with respect to a specific fatigue life. The size of the ellipses varies with the mean stress. As long as the alternating stress (the left side of Equation (17)) is less than or equal to the "safe" limit (the right side of

Equation (17)), the multiaxial stress state will not cause failure of the material within the desired life.

The criterion in Equation (17) can be expressed as a safety factor with respect to the desired life, expressed as follows:

$$D = \frac{S_N - m\bar{\sigma}_m}{\sigma_a} \tag{21}$$

such that when $D < 1.0$, the stress state will result in a shorter than desired fatigue life. If $D \geq 1.0$, the multiaxial stress state will result in a component life greater than or equal to that which is desired. Equation (21) allows one to determine the "safe" range of the alternating effective stress for a given mean hydrostatic stress. If the mean hydrostatic stress is large enough, making the second term in the numerator larger than the first, D cannot be positive, indicating that there is no "safe" range of alternating stress which will produce the desired life.

It should be emphasized that each fatigue life (specified in number of cycles) will result in a new set of constants, S_N and m. Hence, a safety factor can be calculated with respect to any desired fatigue life. Since the sucker rods are designed for indefinite service, the safety factor calculated in the present study was with respect to infinite service life. Although there is no known fatigue threshold data for API Grade C steel, the constants m and S_N can be approximated from the modified Goodman plot shown in Figure 3. Since a safety factor with respect to failure was desired, the full envelope of the Goodman plot was used to derive these constants instead of the more conservative shaded region used by the API. As shown in Figure 3, the amplitude of the reversed stress which will provide an indefinite service life is *T/3*, whereas the amplitude of fluctuating stress which will provide an indefinite service life is *T/4*. Hence, the constants for API Grade C steel evaluate as follows:

$$S_N = \frac{T}{3} = 30\text{ksi} \tag{22}$$

$$m = 3\left(\frac{T/3}{T/4} - 1\right) = 1.0 \tag{23}$$

Thus, the safety factor with respect to failure can be expressed as:

$$D = \frac{30\text{ksi} - \bar{\sigma}_m}{\sigma_a} \tag{24}$$

with respect to indefinite service life. Because Equation (24) is based on approximate constants derived from the modified Goodman diagram rather than actual fatigue data, this criterion should not be interpreted as predicting failure but rather identifying regions with a potential for fatigue failure. In the case of uniaxial loading, Equation (17) with the constants S_N = 30 ksi and m = 1.0 describes the modified Goodman diagram in Figure 3 in terms of mean stress and stress amplitude.

3.3.3 Identification of Critical Fatigue Locations

Figure 17 is a plot of the safety factor with respect to indefinite service life for the 7/8-inch API standard coupling for all the three load cycles under investigation. The plot identifies three regions with a high potential for fatigue damage: at the top of the pin neck, at the root of the first engaged pin thread, and the root of the last engaged box thread. These three locations correspond to the locations of failures observed in field units. Although not as bad as the first two regions, the root of the last engaged box thread does have a high hydrostatic mean stress and a high effective alternating stress relative to the rest of the coupling. A slight change in the geometry or load conditions could make this a more critical location. It is important to understand that regions of high effective stress do not necessarily have a high potential for fatigue failure. Rather, the fatigue damage criterion identifies regions where the effective alternating stress is high relative to the mean hydrostatic stress. Figure 8 shows the distribution of effective stress in the 7/8-inch API coupling at preload as well as the extreme loads. Note that the regions with the highest effective stress do not necessarily correspond to the regions with a high potential for fatigue failure. The distributions of the effective alternating stress and the hydrostatic mean stress are plotted in Figures 18 and 19, respectively. The regions identified with a high potential for fatigue failure also have a high mean hydrostatic stress component (Figure 19) but do not necessarily have the largest alternating effective stress amplitude (Figure 18).

Because the equation for the hydrostatic stress is linear with respect to the principal stresses, the mean hydrostatic stress is always equal to the hydrostatic mean stress. However, because the effective stress equation is nonlinear with respect to the principal stresses, the effective alternating stress (used in Equation 17) is not necessarily equal to the alternating effective stress. In the former, the components of the effective stress equation are the amplitudes of the alternating principal stresses. In the later, the components of the effective stress equation are the principal stresses themselves. The only time that the effective alternating stress will be equal to the alternating effective stress is when the principal stresses increase proportionally, a case called proportional stressing [4]. Figure 20 is a plot of the difference between the effective alternating stress and the alternating effective stress throughout the 7/8-inch API standard coupling for all three load cycles. The plot shows that the difference is small in the areas of interest (the pin neck, the root of the first engaged pin thread, and the root of the last engaged box thread), allowing for the assumption of proportional stressing. The proportional stressing assumption is convenient in that it allows one to look at the effective stress and hydrostatic stress at critical locations throughout the entire load range to determine the "safe" operating range for a coupling. It also simplifies the comparison of different coupling designs. The convenience of this approach will become more clear upon investigation of the simulations performed for this study.

3.3.4 Equivalent Stress at Critical Locations

Figures 21 thru 32 show plots of the effective (von Mises) and hydrostatic stress at the three critical locations identified above as a function of the load applied to the sucker rod. Also identified on these plots are the three different load cycles under investigation: Cycle 1 (-2 ksi to 8 ksi), Cycle 2 (2 ksi to 23 ksi), and Cycle 3 (15 ksi to 30 ksi). Once again, almost all of these plots exhibit the effects of plastic deformation. This is exhibited by a slight change in

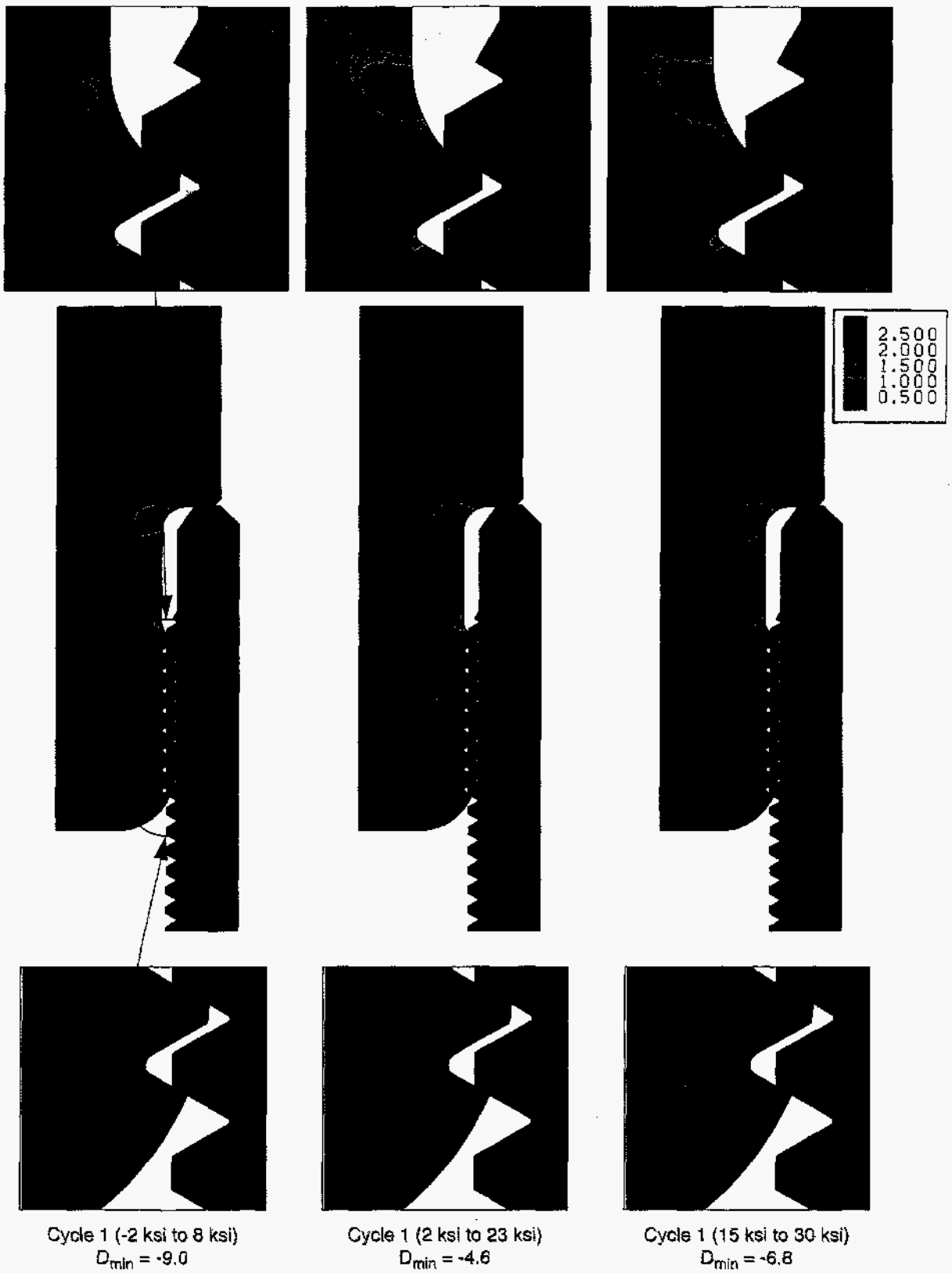

Figure 17. Distribution of the fatigue safety factor with respect to indefinite service life for the 7/8-inch API standard coupling subjected to the three load cycles.

Figure 18. Distribution of the effective alternating stress in the 7/8-inch API standard coupling subjected to the three load cycles.

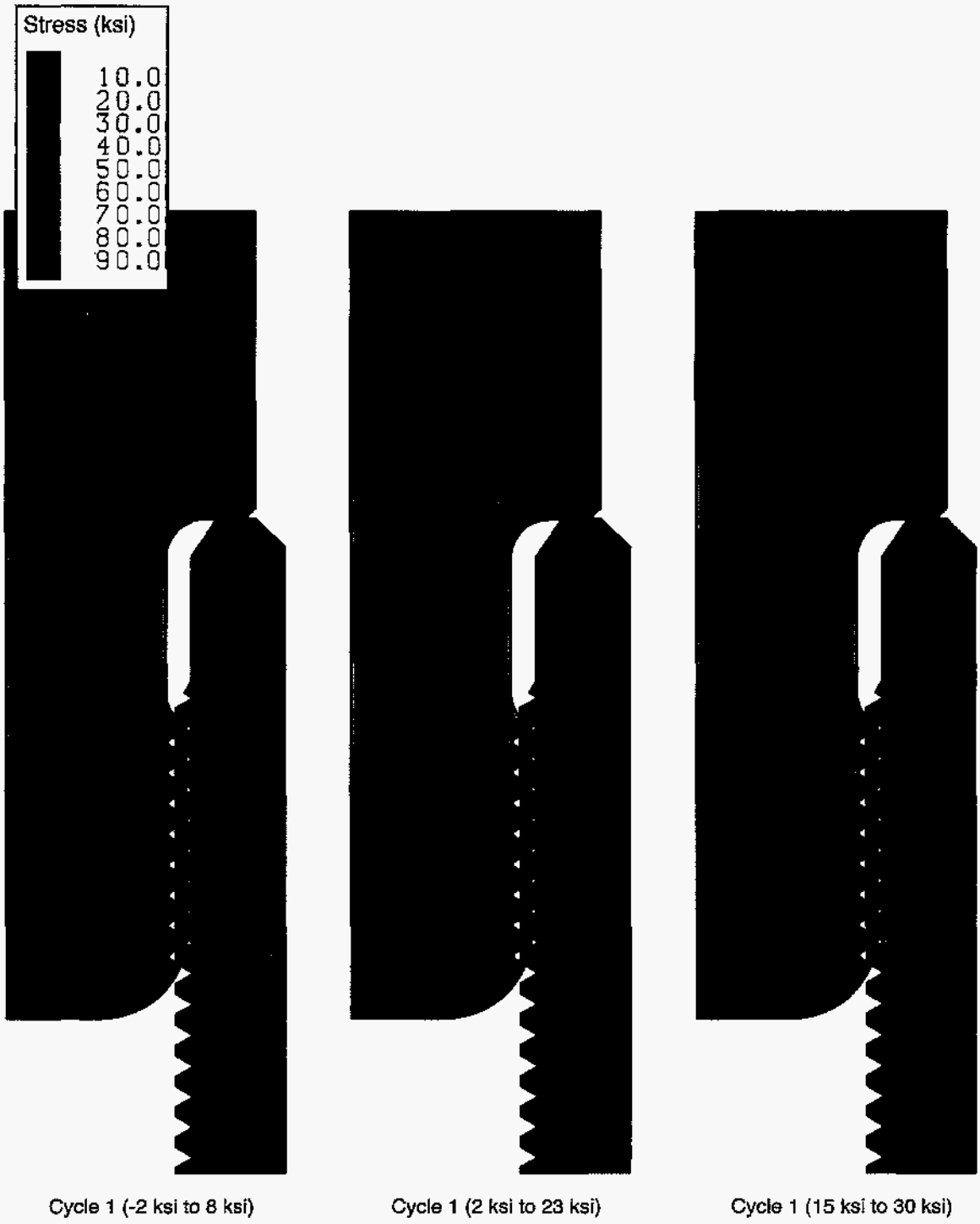

Figure 19. Distribution of the hydrostatic mean stress in the 7/8-inch API standard coupling subjected to the three load cycles.

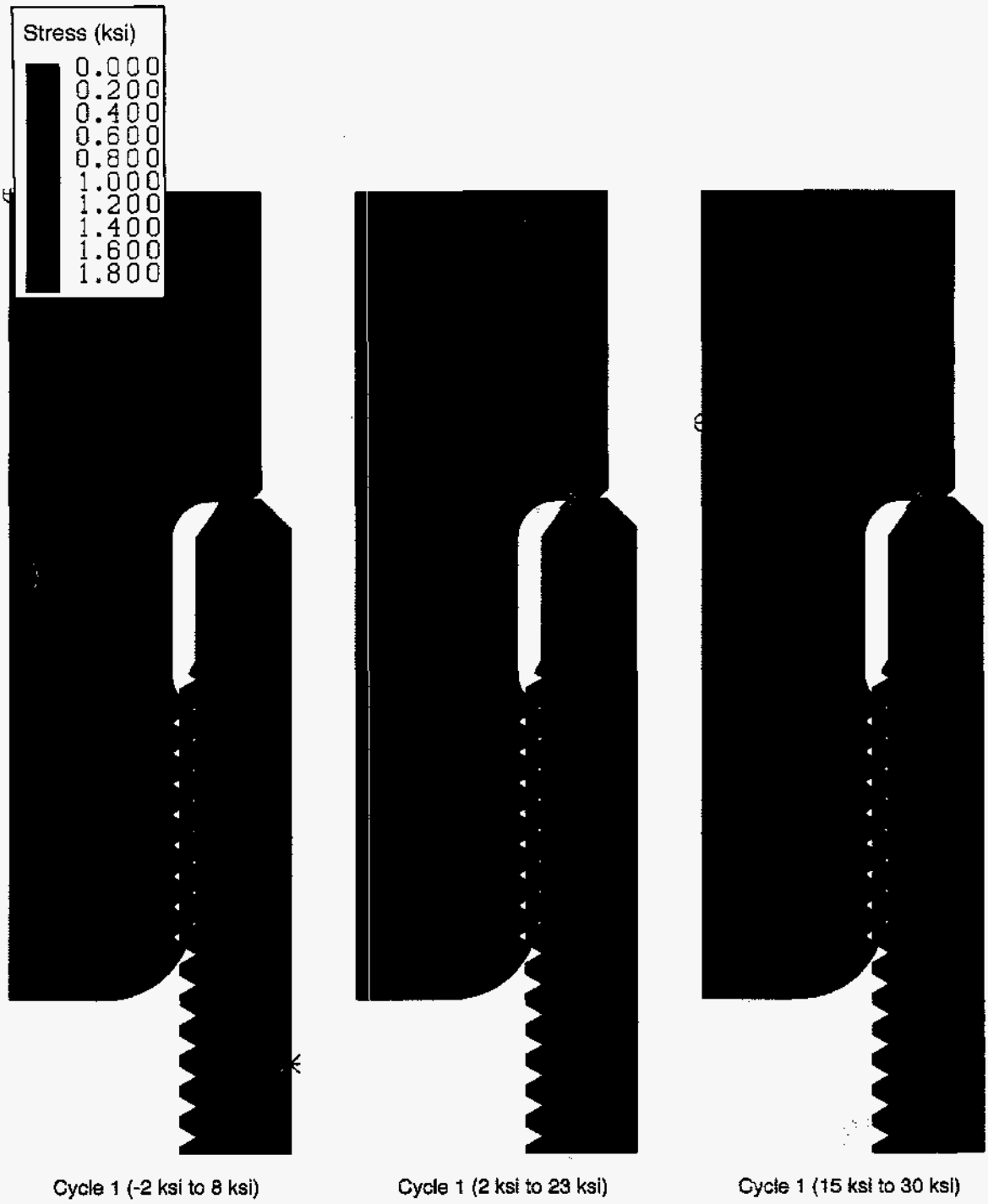

Figure 20. Difference between the effective alternating stress and the alternating effective stress in the 7/8-inch API standard coupling subjected to the three load cycles.

the unloaded state (zero axial load) after the first application of the maximum compression and tension loads. This is typically due to yielding of the pin shoulder and the threads. Hence, the first application of the maximum compression and tensile loads is identified with a dashed line, while the subsequent applied load cycle is identified by a solid line. Because the numerator of Equation (24) must be positive in order for there to exist a "safe" range of alternating stress, the mean hydrostatic stress must be less than the ratio S_N/m, which is 30 ksi for API Grade C steel. Hence, for all locations where the hydrostatic stress is greater than 30 ksi, there exists no allowable stress range which will produce an indefinite life.

Before considering each case, it is useful to discuss how the information presented in the stress plots in Figures 21 thru 32 can be used by a sucker rod designer. Whereas safety factor distribution plots like that shown in Figure 17 provide a "snapshot" of the fatigue potential for a given load cycle, the stress plots in Figures 21 thru 32 permit in-depth investigation of an infinite number of load cycles between -5 ksi and 40 ksi. If fatigue data is available, the stress plots can be used to estimate the service life of the coupling. In this case, the constants S_N and m from Equation (17) can be calculated for various lifetimes (expressed in number of cycles). The information from the stress plots can then be used to calculate the estimated lifetime of each of the three critical locations. Assuming the desired load cycle is known (Cycle 2 for example), then the mean hydrostatic stress is the value of hydrostatic stress at the middle of the cycle (assuming the hydrostatic stress curve is linear over the range of the cycle). The effective stress amplitude is one half of the total change in effective stress over the range of the cycle. These two values can then be used in Equation (17) with various (S_N, m) combinations until the left side of Equation (17) is less than the right. The service life associated with the (S_N, m) pair which satisfies the inequality is the approximate service life at that critical location. The expected coupling life would be the smallest of the estimated lives for the various critical locations. Alternatively, the sucker rod designer can use the stress plots to back out the load cycles which will provide a desired service life. In this case, the constants (S_N, m) corresponding to the desired service life can be used in Equation (17) to determine the allowable effective stress amplitude for a given mean hydrostatic stress. The designer can then use the stress plots to extract the corresponding minimum and maximum loads to be applied to the sucker rods.

In the absence of fatigue data, the stress plots can be used to compare the relative performance of various coupling designs and make-ups. This is how the information will be used in the following discussion. Hence, the specific cases are grouped logically to facilitate direct comparison. For a given load cycle, several characteristics of the stress plots provide meaningful information for comparison of the various analysis cases. First, the slope of the effective stress curve is more significant than the absolute magnitude since the slope is directly proportional to the effective stress amplitude over any given load cycle. The greater the slope, the higher the effective stress amplitude. Hence, the terms "stress amplitude" and "slope" are used interchangeably in the following discussion of the results. Second, the absolute magnitude of the hydrostatic stress at the middle of a given load cycle is very important. The smaller the mean hydrostatic stress, the greater the allowable alternating effective stress. If, for example, Coupling A has both a higher mean hydrostatic stress and its effective stress plot has a greater slope (i.e. a higher effective stress amplitude) than Coupling B, then Coupling A will have a shorter service life. It is difficult to assess how much shorter

without actual fatigue data. As Figure 15 illustrates, even small differences in the mean hydrostatic stress or effective stress amplitude can result in large differences in service life.

Root of First Engaged Pin Thread

Figure 21 shows the effective and hydrostatic stress ranges in the root of the first engaged pin thread for the 3/4, 7/8, and 1-inch API couplings. Since the hydrostatic stress of all three couplings is greater than 30 ksi over the entire load range, all three couplings are predicted to have a finite life. Of the three coupling sizes, the 1-inch coupling exhibits the smallest effective stress amplitude over the range of applied loads, while the 7/8-inch coupling exhibits the largest effective stress amplitude. Note that the slopes of the effective stress curves are consistent with the load partitioning factors presented in Table 3. Since the hydrostatic stress is nearly the same for all three coupling sizes, the 1-inch coupling will probably have a longer service life than the other two coupling sizes.

Figure 22 shows the effective and hydrostatic stress ranges in the root of the first engaged pin thread for the 7/8-inch API coupling with make-ups of 0.0, 1.0, and 1.5. For all three load cycles, the made-up couplings have a higher hydrostatic stress but a smaller effective stress amplitude than the coupling which is not made-up. The made-up joints have a higher mean hydrostatic stress because they are preloaded, meaning this location is stressed even when there is no applied axial load. The joint which is not made-up separates immediately upon tensile loading, which is why the slope of the effective stress plot is higher. Interestingly, the joint which is not made-up should provide an indefinite service life with respect to failure at this location, whereas the two made-up joints are predicted to have a finite life at this location. (The problem with the joint which is not made-up is that it will continue to loosen and eventually uncouple.) Finally, the plot shows that the additional make-up of 1.5 over 1.0 does not have any effect on the fatigue life of the first engaged pin thread. This plateau with respect to make-up is due to yielding of the pin threads and shoulder.

Figure 23 shows the effective and hydrostatic stress ranges in the root of the first engaged pin thread for various combinations of the Flexbar (FB), slimhole (SH), and Spiralock (SL) modifications to the base coupling (S7). The Flexbar and slimhole modifications to the base geometry produce small changes in the hydrostatic and effective stress for all three load cycles. However, as previously mentioned, small changes in the mean hydrostatic stress or effective stress amplitude can have significant effects of fatigue life. The incorporation of the Spiralock threads produces a significant reduction in the hydrostatic stress for all three load cycles. This occurs because the Spiralock threads reduced the preload in a fully made-up coupling (see Figure 13). However, the slope of the Spiralock effective stress curve is greater than that of the API couplings for applied loads greater than approximately 7 ksi. This is the load at which the Spiralock couplings separate. Recall that when the coupling separates the pin takes the entire axial load, and the load partitioning factor (γ_p) increases to one. This is evidenced by an increase in slope of the pin load diagram (Figure 13), which translates into an increase in the stress range over the same load range. Once again, the slimhole and Flexbar modifications to the Spiralock coupling have no significant effect on the performance of the Spiralock coupling.

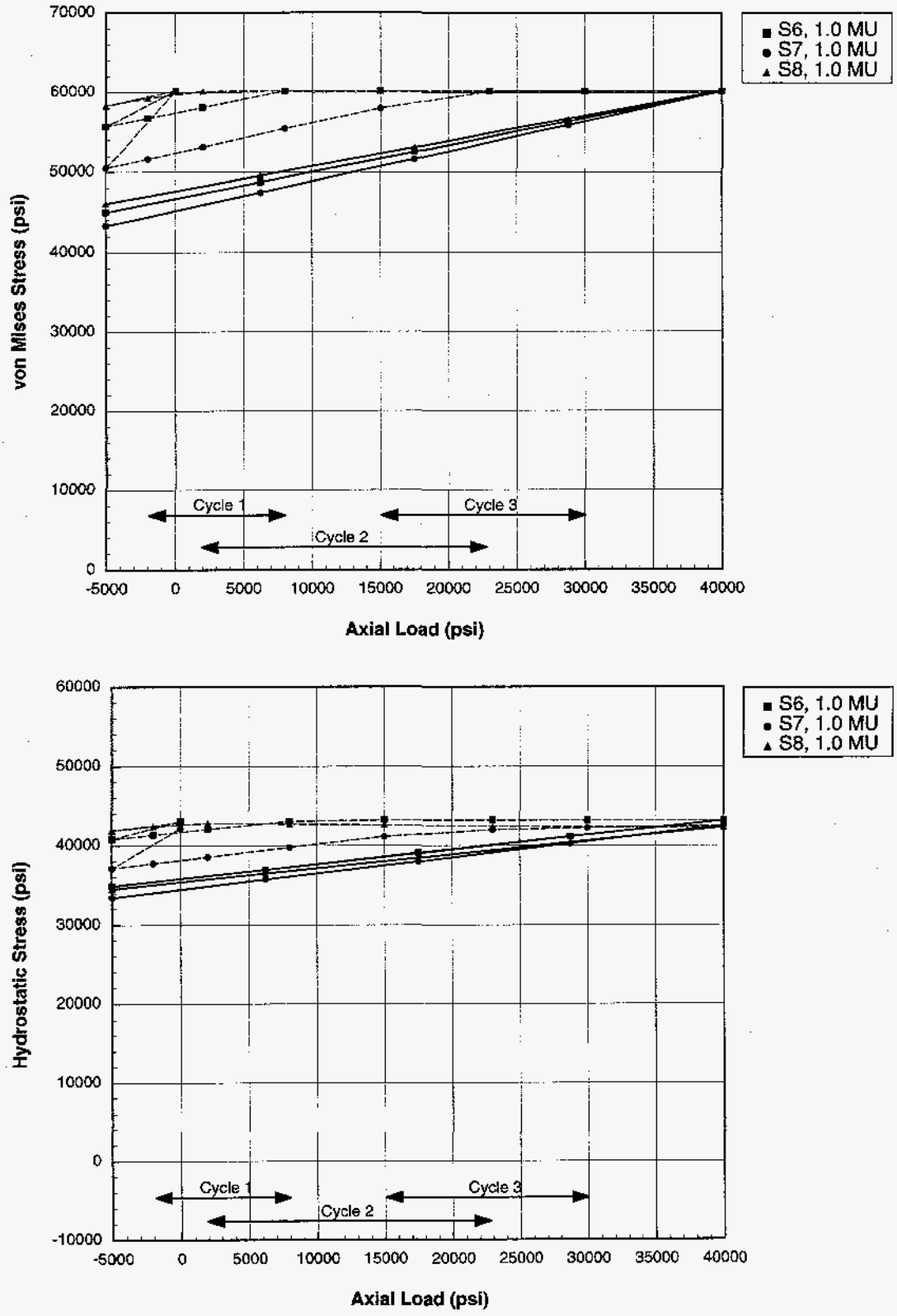

Figure 21. Von Mises and hydrostatic stress at the root of the first engaged pin thread as a function of applied axial load for various coupling sizes.

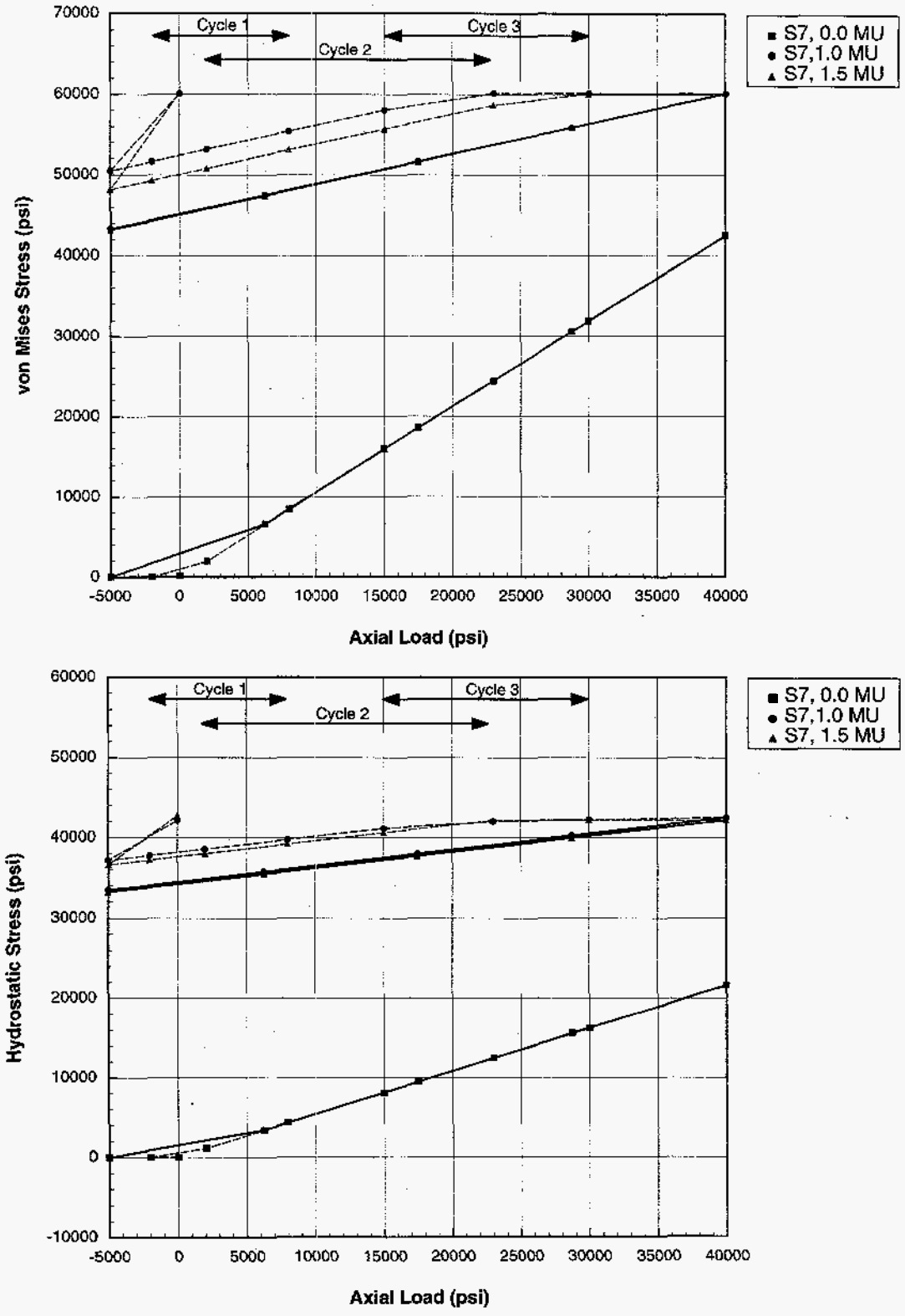

Figure 22. Von Mises and hydrostatic stress at the root of the first engaged pin thread as a function of applied axial load for various make-ups of the 7/8-inch API coupling.

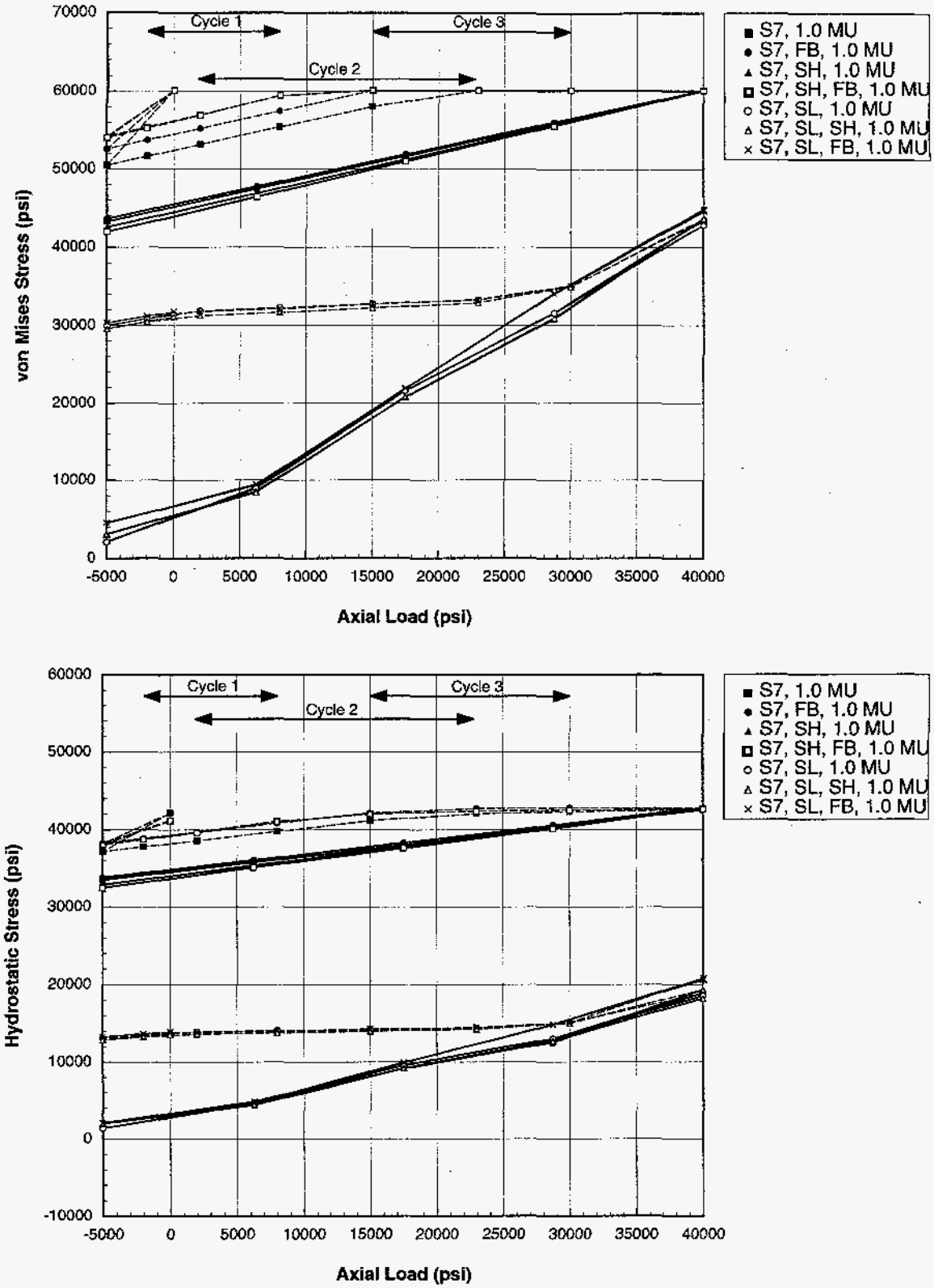

Figure 23. Von Mises and hydrostatic stress at the root of the first engaged pin thread as a function of applied axial load for various combinations of the Flexbar (FB), slimhole (SH), and Spiralock (SL) modifications to the base coupling (S7).

Figure 24 shows the effective and hydrostatic stress ranges in the root of the first engaged pin thread of a Spiralock coupling with make-ups of 0.0, 1.0, 1.5, 2.0, 2.5, and 3.0. Again, the effective stress amplitude increases when the coupling separates (the cases with make-ups of 0.0 and 1.0). That is why the slope of the 0.0 and 1.0 make-up curves is larger than those with make-ups of 1.5 and greater. As the make-up increases above 1.5, the effective stress amplitude over any of the three cycles stays the same (i.e. the slopes of the curves are the same), while the mean hydrostatic stress increases. This increase in the hydrostatic stress will shorten the service life in this region. Further increases in the make-up over 2.0 produce no significant changes in either the effective or hydrostatic stress. This plateau is due to yielding of the threads during preload. In summary, the Spiralock thread form with a make-up of 1.5 appears to offer an improvement over the standard API coupling (1.0 MU) with respect to minimizing both the mean hydrostatic stress and the effective stress amplitude in the root of the first engaged thread. This is true for all three load cycles. However, if the coupling is over tightened (make-ups greater than or equal to 2.0), then the performance is very similar to the base 7/8-inch API coupling.

Pin Neck

All of the above comments made for the stress range in the first engaged pin thread also apply to the plots for the pin neck (Figures 25 thru 28) since the fatigue performance at this location exhibit the same dependencies on the design parameters. Hence, the discussion of the results at this location may seem slightly repetitive. Figure 25 shows the effective and hydrostatic stress ranges in the pin neck for the 3/4, 7/8, and 1-inch API couplings. The effective stress amplitude decreases as the coupling size increases, while the mean stress increases with coupling size. Once again, note that the slopes of the effective stress curves are consistent with the load partitioning factors presented in Table 3. Since the mean hydrostatic stress is greater than 30 ksi over the entire load range, all three coupling sizes are predicted to have a finite life in the pin neck region. Fatigue data would be required to accurately determine the differences in fatigue life of the three coupling sizes.

Figure 26 shows the effect of make-up on the stress range in the pin neck. No make-up results in the pin carrying the entire axial load. Hence, the effective stress amplitude in the unmade-up coupling is quite large compared to the cases which are made-up. However, make-up has the effect of increasing the hydrostatic stress in this region which decreases the fatigue life. The hydrostatic stress of the unmade-up joint is less than 30 ksi over the entire load range. Hence, for every mean stress there exists an alternating effective stress which provide indefinite service life. In the case of the made-up joints, the hydrostatic stress is greater than 30 ksi over the entire load range. Hence, both of the made-up joints will have a finite service life for any load cycle in this range. Further increases in make-up over 1.0 provide no significant change to either the effective stress amplitude or mean hydrostatic stress in the pin neck.

The most effective method for increasing the fatigue life of a component is to decrease the severity of the stress concentration. The Flexbar modification to the standard API coupling was designed to decrease the severity of the stress concentration in the pin neck. Figure 27 shows that the Flexbar modification reduces both the mean hydrostatic stress and effective stress amplitude in the pin neck for any of the three cycles. Since the effective stress curve for

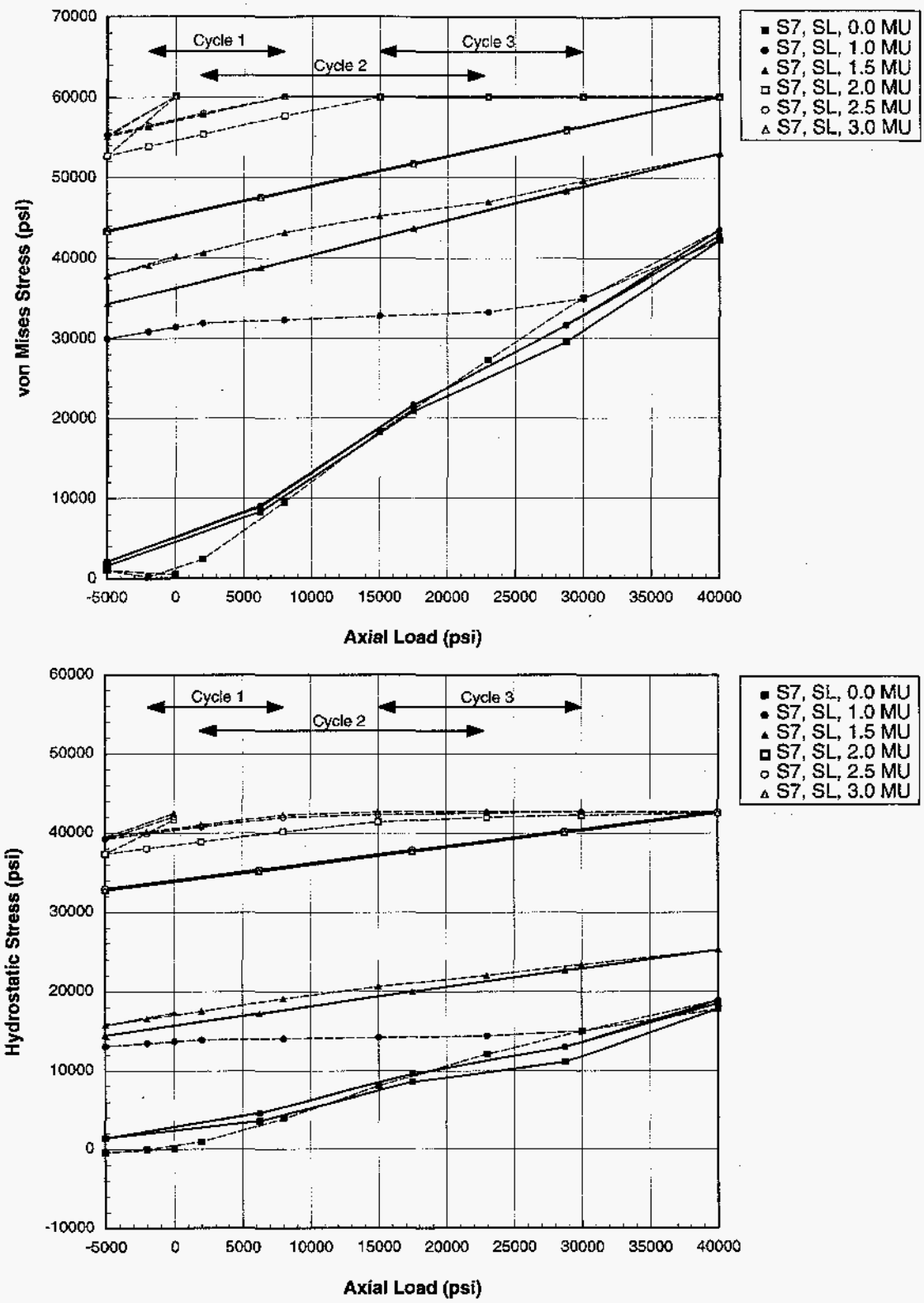

Figure 24. Von Mises and hydrostatic stress at the root of the first engaged pin thread as a function of applied axial load for the Spiralock coupling with make-ups of 0.0, 1.0, 1.5, 2.0, 2.5, and 3.0.

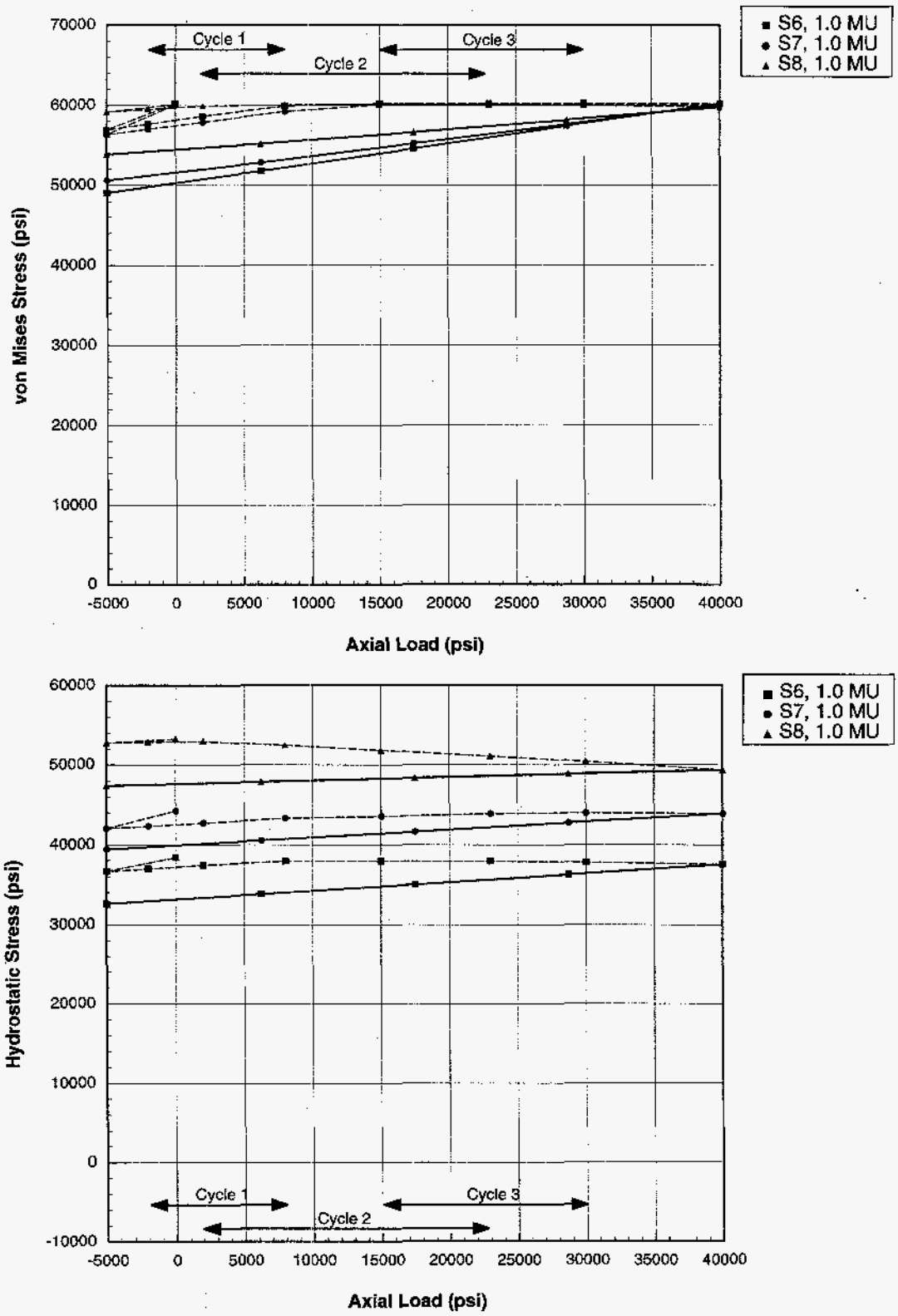

Figure 25. Von Mises and hydrostatic stress at the pin neck as a function of applied axial load for various coupling sizes.

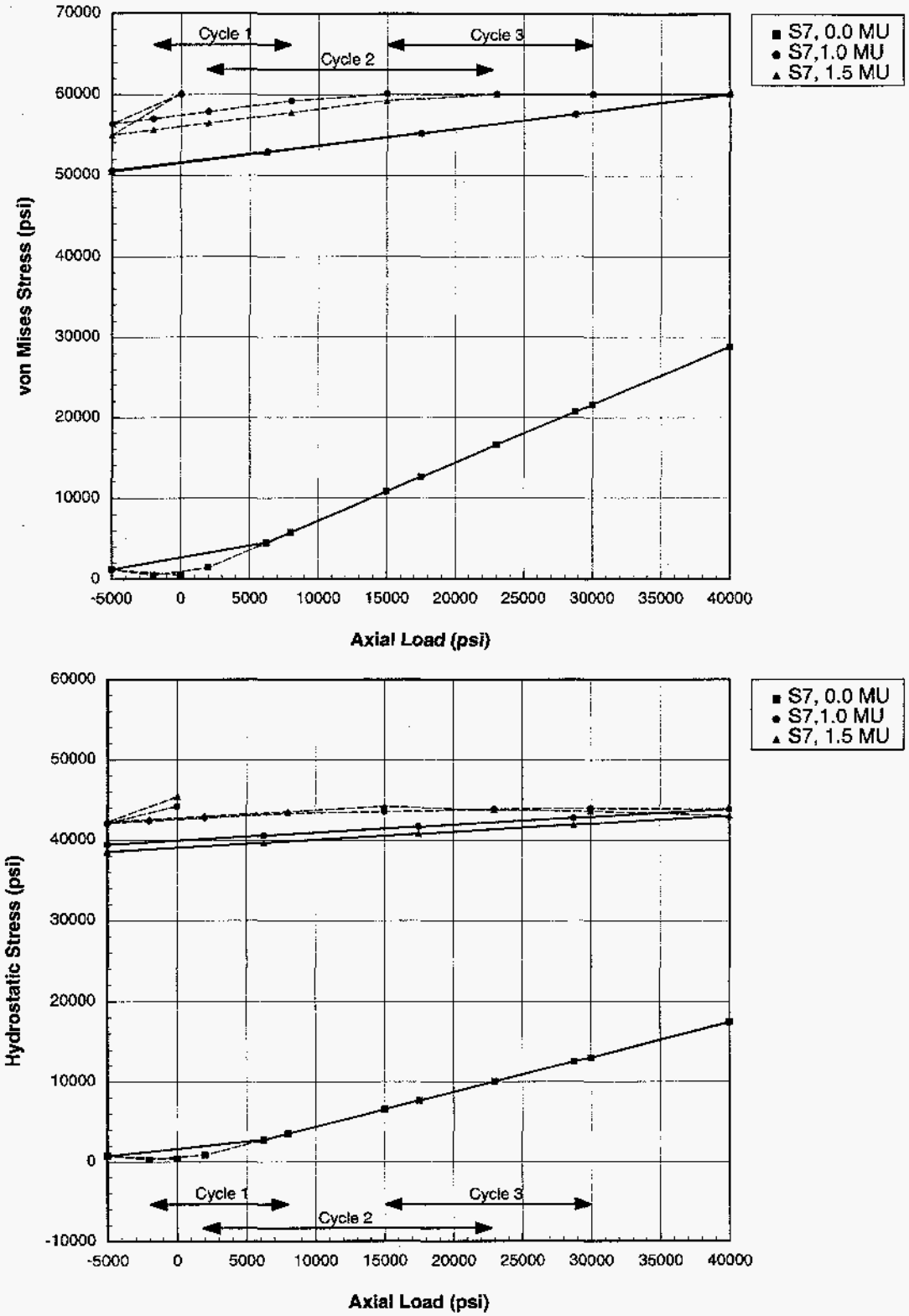

Figure 26. Von Mises and hydrostatic stress at the pin neck as a function of applied axial load for various make-ups of the 7/8-inch API coupling.

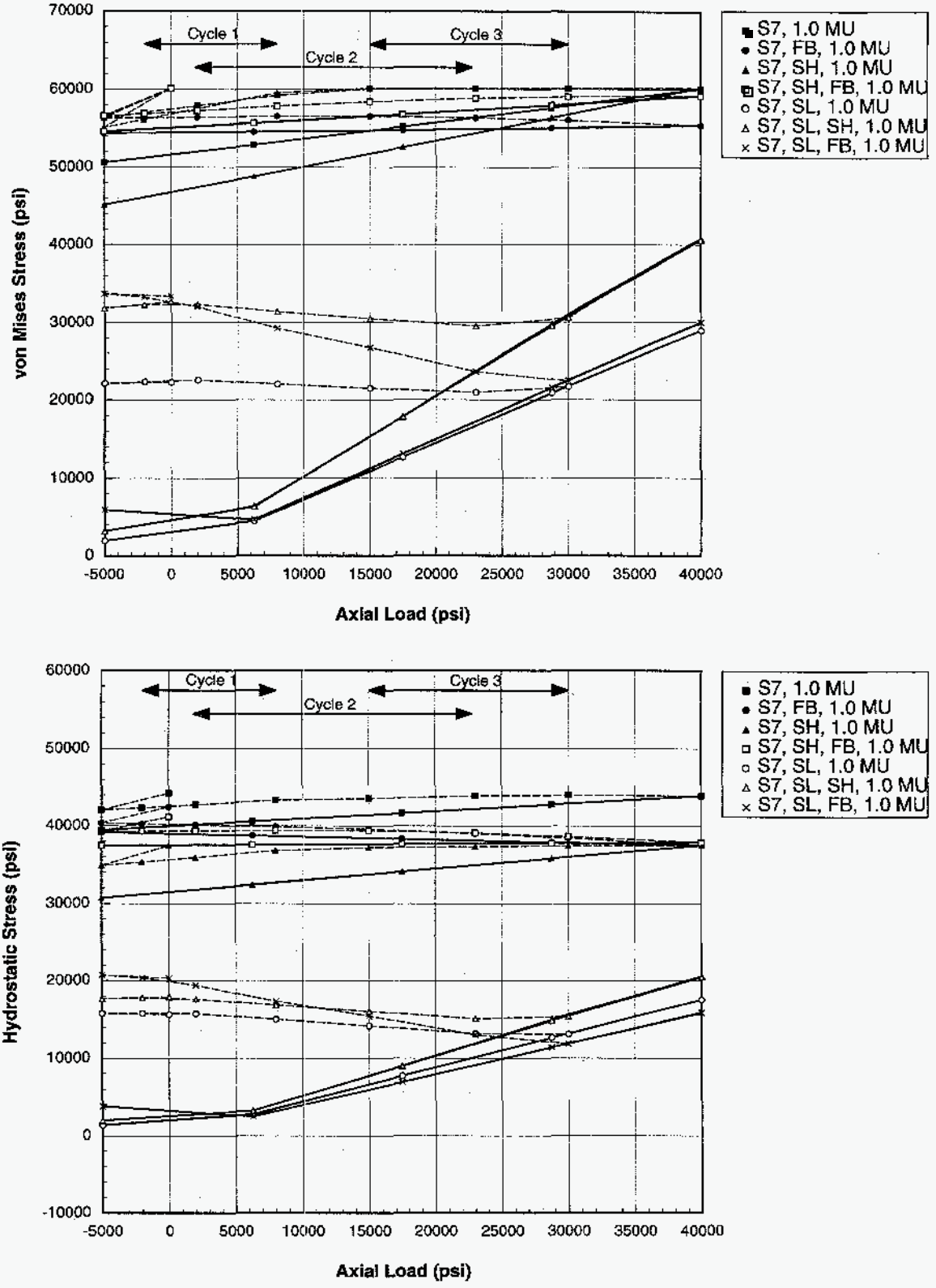

Figure 27. Von Mises and hydrostatic stress at the pin neck as a function of applied axial load for various combinations of the Flexbar (FB), slimhole (SH), and Spiralock (SL) modifications to the base coupling (S7).

the Flexbar coupling (S7, FB, 1.0 MU) is nearly flat, the stress amplitude is almost zero. Hence, the Flexbar modification should extend the service life in the neck region of the 7/8-inch coupling. However, since the hydrostatic stress is still greater than 30 ksi over the entire load range, the Flexbar coupling is still predicted to have a finite life.

The slimhole modification, also shown in Figure 27, reduces the mean hydrostatic stress due to a decrease in the preload capacity of the slimhole couplings (as seen in Figure 13). However, the effective stress amplitude increases over the three load cycles due to the fact that the slimhole coupling is not as stiff as the standard coupling (hence γ_p is larger). The reduced stiffness results in more of the applied load being carried by the pin (see Section 3.2). The slimhole coupling will probably have a longer service life (in the pin neck) since the reduction in mean hydrostatic stress is greater than the increase in effective stress amplitude. Finally, the Flexbar modification with the slimhole coupling reduces the effective stress amplitude over the three load cycles, yet increases the mean hydrostatic stress slightly. Once again, fatigue data will be required to perform accurate service life estimates.

The incorporation of the Spiralock threads, shown in Figure 27, produces a significant reduction in the hydrostatic stress for all three load cycles. This occurs because the Spiralock threads reduced the preload in a fully made-up coupling. As was the case for the pin thread region, the slope of the Spiralock effective stress curve is greater than that of the API couplings for applied loads greater than approximately 7 ksi. This is the load at which the Spiralock coupling separates, increasing the load partitioning factor (γ_p) to one. As a result, the effective stress amplitude increases substantially after separation occurs.

Figure 28 shows the effective and hydrostatic stress ranges in the pin neck of a Spiralock coupling with make-ups of 0.0, 1.0, 1.5, 2.0, 2.5, and 3.0. The pin neck exhibits the same behavior as the first engaged thread for the same reasons sited in the previous section. This figure shows that the Spiralock couplings must be sufficiently made-up to avoid the high effective stress amplitudes associated with coupling separation. Compared to the 7/8-inch API coupling, the Spiralock coupling with a make-up of 1.5 reduces both the mean hydrostatic stress and the effective stress amplitude in pin neck. If overtightened (make-ups greater than or equal to 2.0), the coupling performs similar to the 7/8-inch API coupling.

Root of Last Engaged Box Thread

Figure 29 shows the effective and hydrostatic stress plots in the root of the last engaged box thread for the 3/4, 7/8, and 1-inch API couplings. At zero axial load (or preload), all three couplings exhibit a finite amount of stress. This indicates that there is load transfer between all of the threads, even this far from the first engaged thread. Furthermore, the effective stress amplitude (or slope) at this location is significantly greater than that predicted at the first engaged thread (Figure 21) or the pin neck (Figure 25). This was expected since the material in this region of the box section, not benefiting as greatly from preload, is subjected to the full range of the applied axial load. Hence, the slopes of the effective stress curves are fairly constant between the sizes and are not consistent with the load partitioning factors presented in Table 3. Since the hydrostatic stress in the 1-inch coupling is greater than 30 ksi for all positive loads, this region of the 1-inch coupling is predicted to have a finite life. For the 3/4 and 7/8 inch couplings, the hydrostatic stress is less that 30 ksi for axial loads up to 17 ksi.

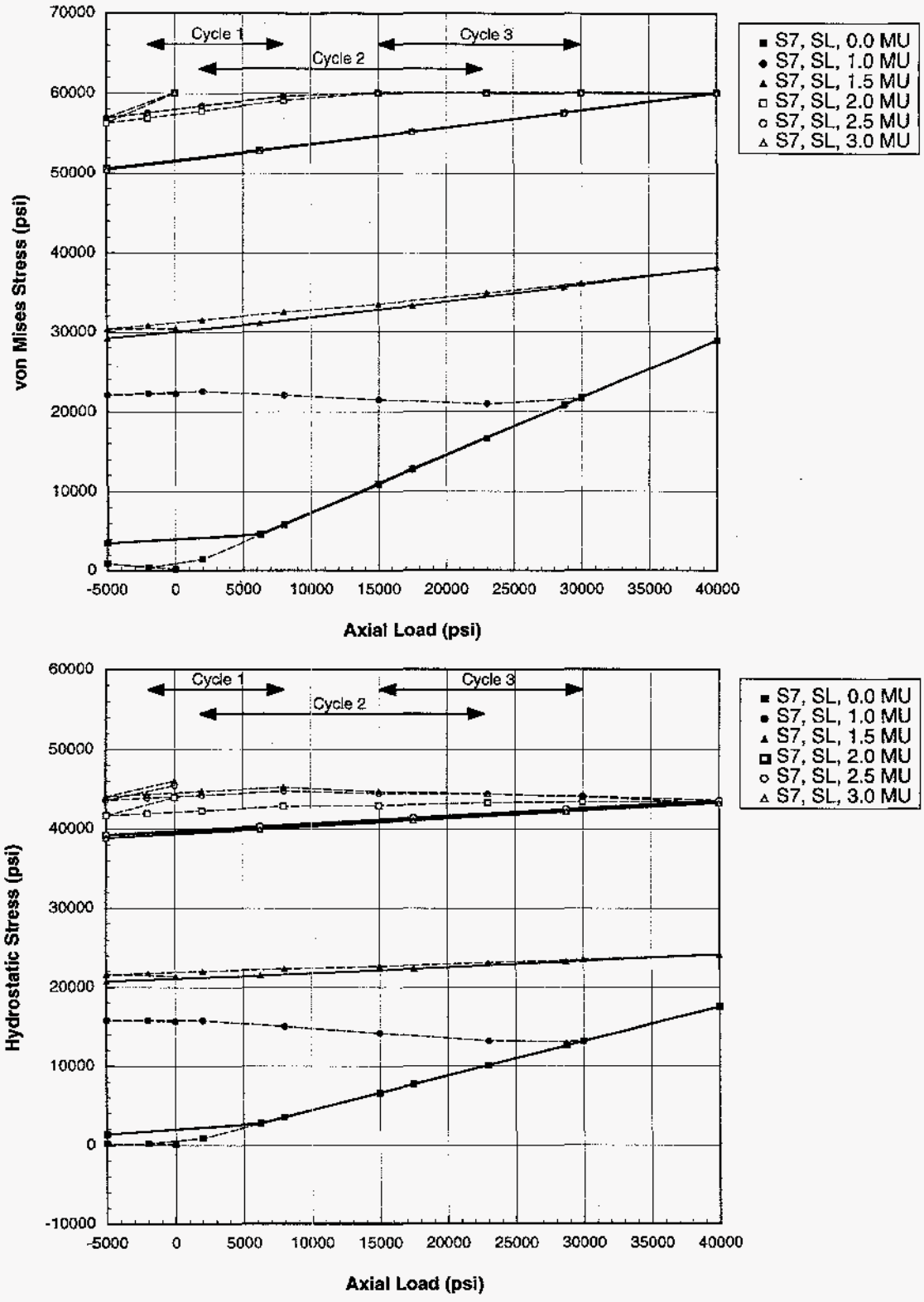

Figure 28. Von Mises and hydrostatic stress at the pin neck as a function of applied axial load for the Spiralock coupling with make-ups of 0.0, 1.0, 1.5, 2.0, 2.5, and 3.0.

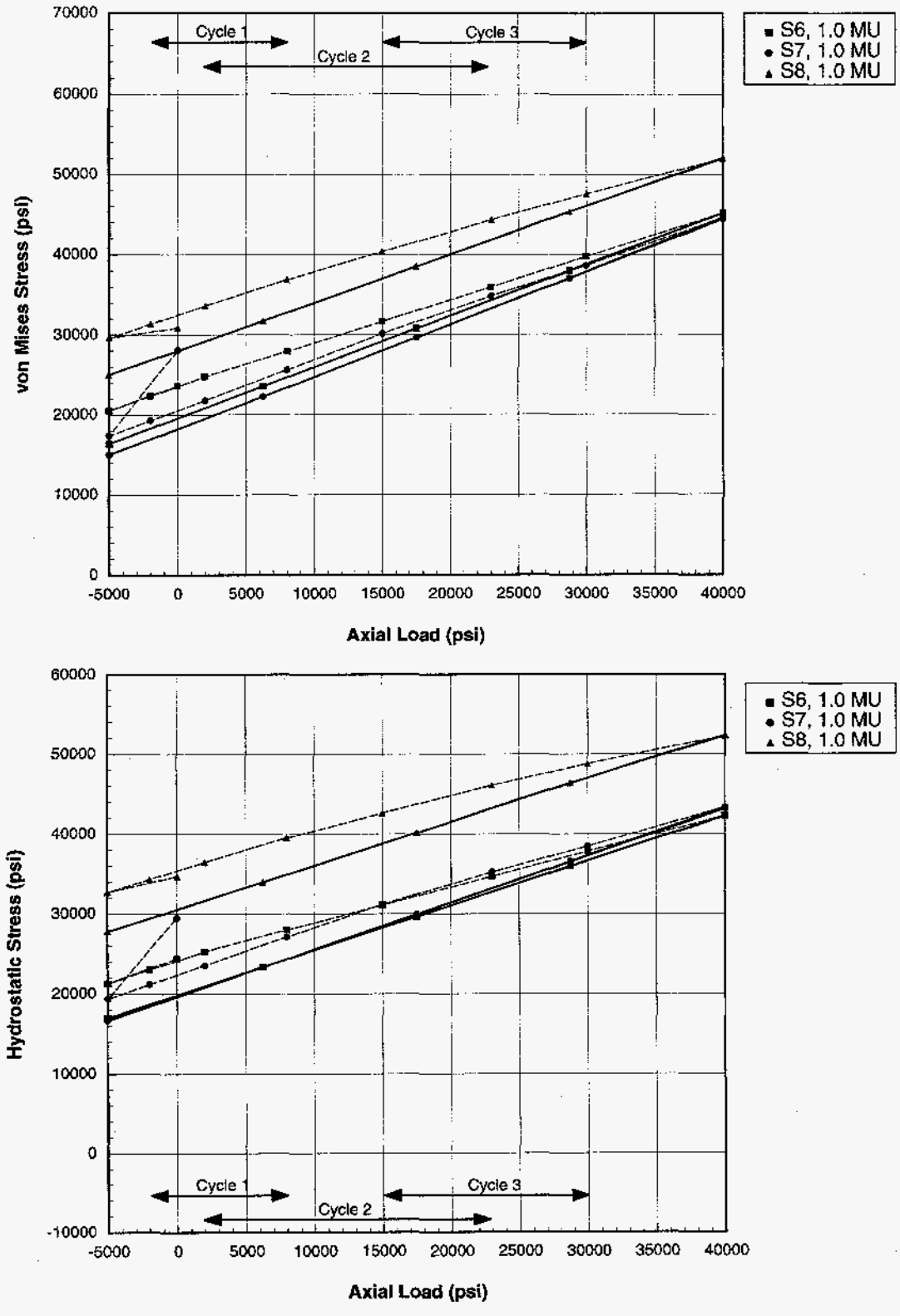

Figure 29. Von Mises and hydrostatic stress at the root of the last engaged box thread as a function of applied axial load for various coupling sizes.

Hence, the safety factor (D) will be greater than one in Cycle 1, but less than one for Cycles 2 and 3. This is a good example of a marginal region for which the design loads can be tailored to improve the fatigue life.

Figure 30 shows the stress range in the root of the last engaged box thread for the 7/8-inch API coupling with make-ups of 0.0, 1.0, and 1.5. As the plot shows, the made-up couplings have a greater mean hydrostatic stress than the coupling which is not made-up. However, unlike the first engaged pin thread (Figure 22), the effective stress amplitude in the last engaged thread is not significantly affected by the amount of preload in the coupling (i.e. the slope does not change much for the made-up couplings). Again, this is due to the fact that the material in this region of the box section is subjected to nearly the full range of the applied axial load, regardless of the coupling preload. Hence, because preload elevates the mean stress in the last engaged box thread, coupling make-up actually will reduce the fatigue life of the coupling. Consider Cycle 3 for example, the 7/8-inch API coupling with no make-up will have a safety factor greater than one, whereas the safety factor drops to less than one with a makeup of 1.0. Again, the problem with no make-up is that the coupling will loosen and eventually separate. Notice that for the made-up joints the effective stress amplitude at the last engaged box thread is significantly greater than that predicted at the first engaged pin thread (Figure 22) or the pin neck (Figure 26). However, for the coupling which has no make-up, the effective stress amplitudes in all three locations are nearly equal.

Figure 31 shows the stress range in the root of the last engaged box thread for various combinations of the Flexbar (FB), Spiralock (SL), and slimhole (SH) geometry modifications to the base geometry (S7). The Flexbar modification produces very little change in the effective stress amplitude or the mean hydrostatic stress for any of the three load cycles identified on the plots. This was expected since the Flexbar modification merely increases the grip length of the coupling, but does not change the thread pattern of the pin and box sections. The largest stress amplitude is predicted for the slimhole couplings. Because the slimhole couplings have a box section with a smaller cross-sectional area, the stress amplitude is larger than that of the base (S7) coupling. Hence, the stress amplitude in the last engaged thread will also be larger. In the three Spiralock cases, the mean hydrostatic stress in the last engaged root thread is significantly smaller than the base (S7) coupling. This is due to the fact that the preload in these couplings is significantly reduced by thread yielding (see Figure 13). However, the effective stress amplitude is much larger due to the fact that these couplings separate at low axial loads (approximately 7 ksi). Once again, in all cases, the effective stress amplitude at the last engaged box thread is greater than that predicted at the first engaged pin thread (Figure 23) or the pin neck (Figure 27) due to the fact that this section of the box is subjected to the full range of the applied load.

Figure 32 shows the stress range in the root of the last engaged box thread for the Spiralock coupling with make-ups of 0.0, 1.0, 1.5, 2.0, 2.5, and 3.0. The Spiralock coupling separates with make-ups of 0.0 and 1.0. Once separation occurs, the pin carries the entire axial load. This is evident in Figure 32, where the slope of the stress curve increases at the point at which separation occurs. Once again, Figure 32 shows that the Spiralock couplings must be sufficiently made-up to avoid the high effective stress amplitudes associated with coupling separation. Compared to the 7/8-inch API coupling, the Spiralock coupling with a make-up of

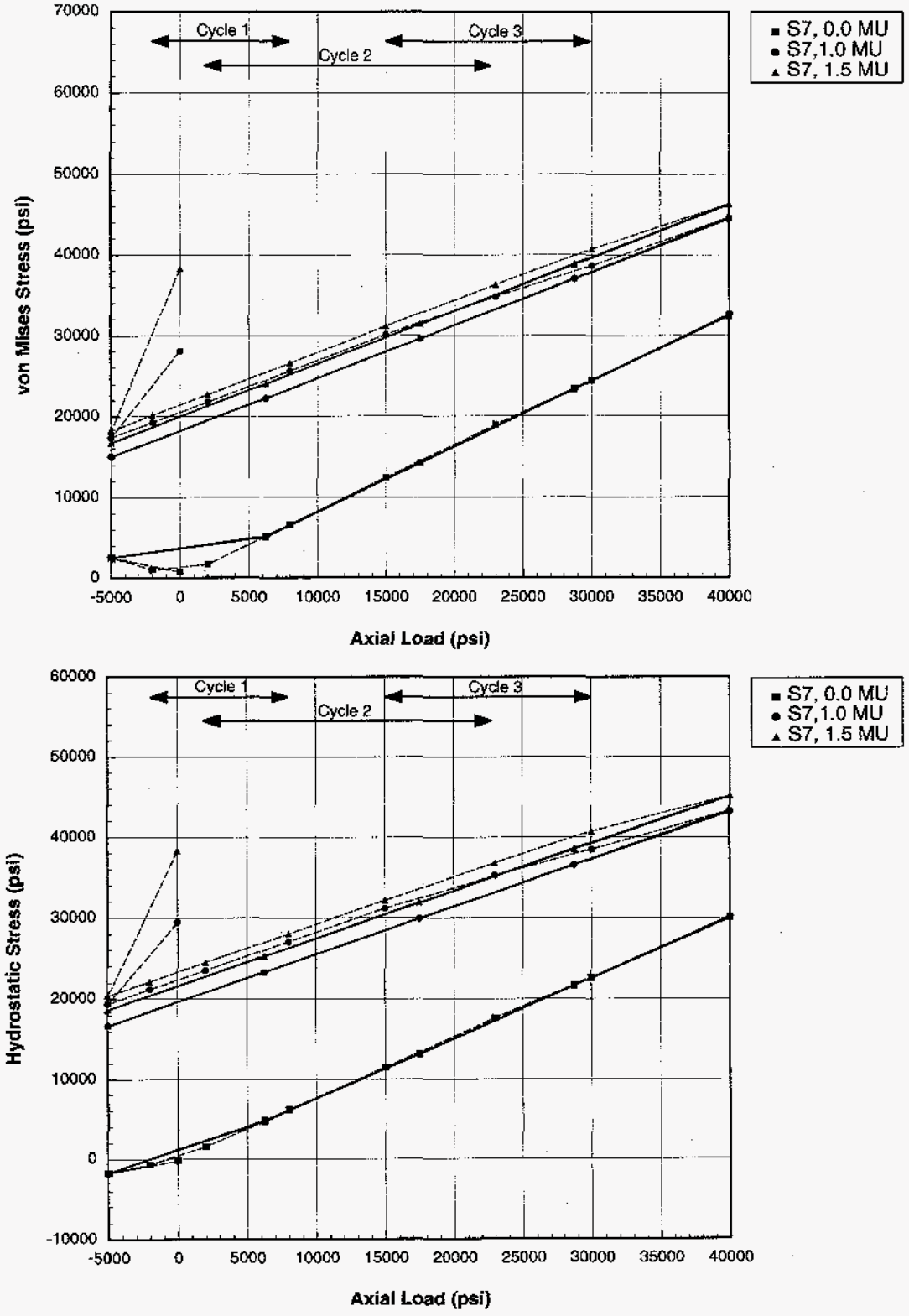

Figure 30. Von Mises and hydrostatic stress at the root of the last engaged box thread as a function of applied axial load for various make-ups of the 7/8-inch API coupling.

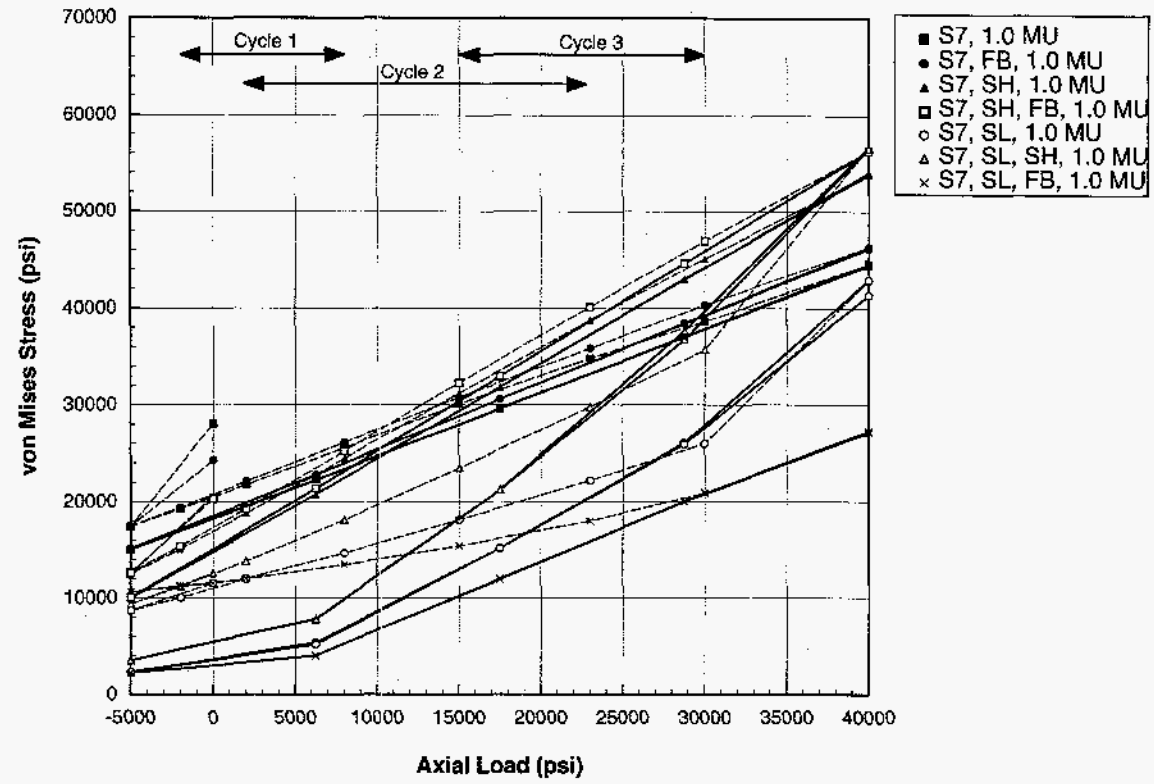

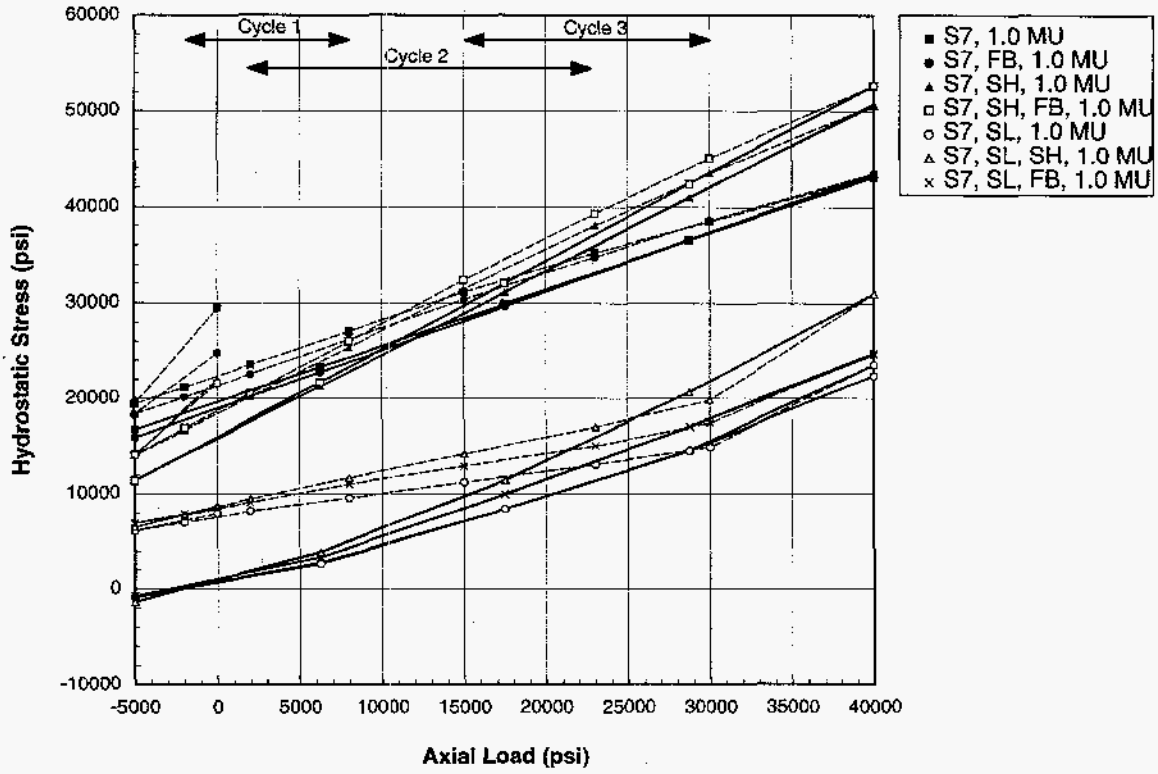

Figure 31. Von Mises and hydrostatic stress at the root of the last engaged box thread as a function of applied axial load for various combinations of the Flexbar (FB), slimhole (SH), and Spiralock (SL) modifications to the base coupling (S7).

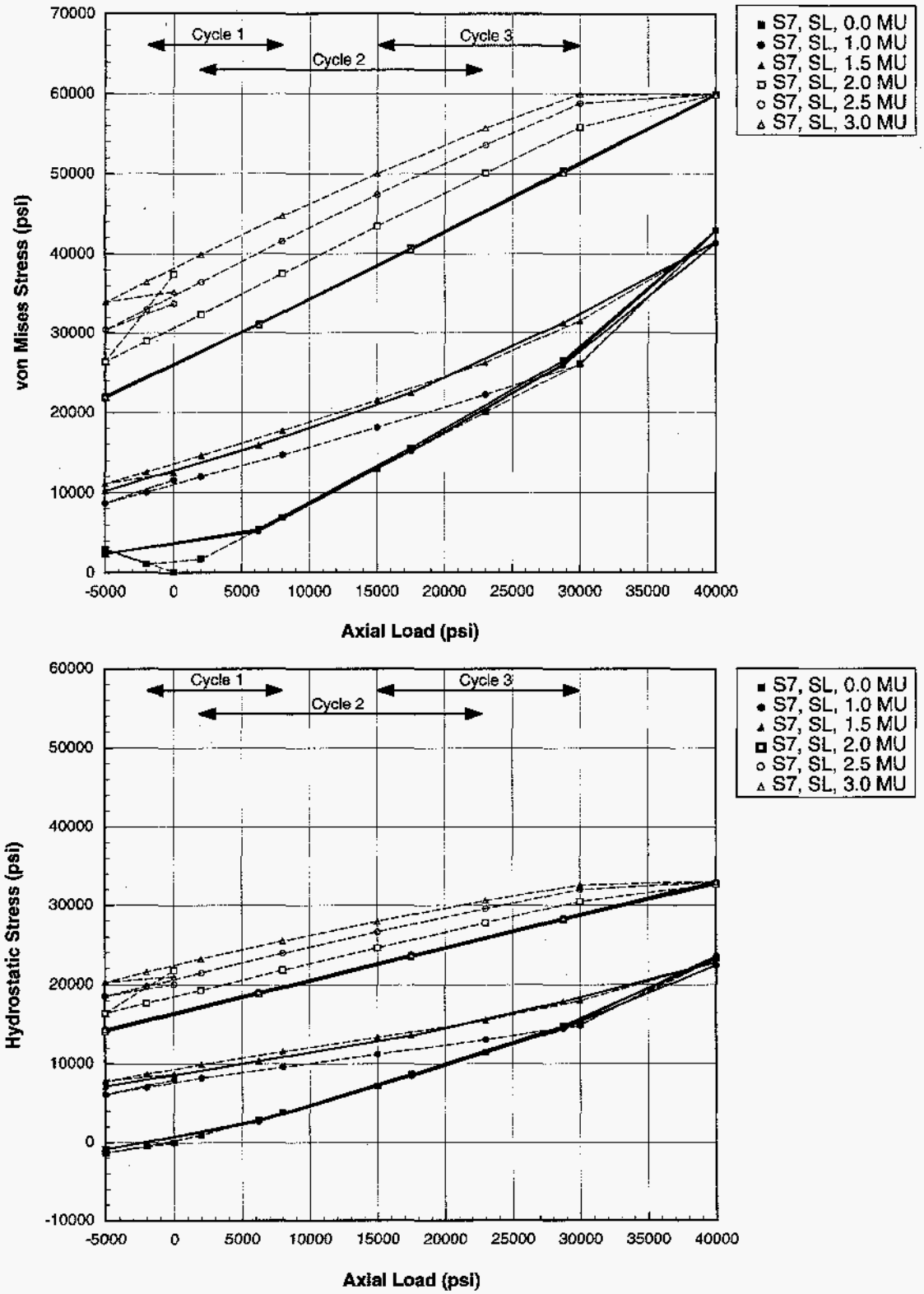

Figure 32. Von Mises and hydrostatic stress at the root of the last engaged box thread as a function of applied axial load for the Spiralock coupling with make-ups of 0.0, 1.0, 1.5, 2.0, 2.5, and 3.0.

1.5 reduces the mean hydrostatic stress in the last engaged box thread, while the effective stress amplitude at this location is about the same in both couplings. At higher make-ups (2.0 and greater), the mean hydrostatic stress of the Spiralock coupling is still significantly lower than that of the API coupling, but the effective stress amplitude is greater.

3.3.5 Effect of Make-up on Service Life

Based on the stress plots presented in the previous section, the Spiralock coupling is predicted to have a longer service life than an equivalent API standard coupling. This longer service life is attributed to the lower hydrostatic mean stress throughout the coupling, which is due to a reduction in preload for a standard make-up of 1.0. The reduced preload was achieved because the Spiralock threads yield more during make-up. As stated previously, the yielding of the Spiralock threads is due to very localized point contact between the pin and box threads. This point contact generates very high stresses in the pin threads, causing them to yield at lower make-ups. Hence, the Spiralock threads function as a preload limiter which will extend the service life of the coupling.

The stress plots for the three critical regions suggest that there is an optimum make-up. The couplings must be sufficiently made-up to avoid the high effective stress amplitudes associated with coupling separation. Yet the couplings should not be overtightened, as additional make-up increases the mean hydrostatic stress in the coupling which reduces fatigue life. This point was illustrated in the previous section for the Spiralock coupling. Compared to the 7/8-inch API standard coupling, the Spiralock coupling with a make-up of 1.5 reduces both the mean hydrostatic stress and the effective stress amplitude at all three critical locations. If too loose, the coupling separated and the slope of the effective stress plot increased. If too tight (make-ups greater than or equal to 2.0), the coupling performed similar to the 7/8-inch API coupling. To better illustrate the effect of make-up on fatigue life, Figure 33 shows the distribution of the fatigue safety factor (with respect to indefinite service life) in the 7/8-inch Spiralock coupling (with make-ups of 1.0, 1.5, and 2.0) subjected to the entire load range (-5 ksi to 40 ksi). Although the load range is more extreme than sucker rod couplings are typically subjected to, the plot illustrates that there is an optimum make-up which will maximize the fatigue life of a sucker rod coupling. At a make-up of 1.5, the fatigue affected regions are small and the minimum safety factor is 0.8. If too loose (1.0 MU), the affected regions increase in size and the minimum safety factor decreases to 0.7. If the coupling is too tight (2.0 MU), the affected regions increase in size and the minimum safety factor decreases to -2.1 (the negative implies there is no "safe" amplitude of effective stress). Hence, the optimum make-up is that which is just enough to avoid coupling separation during the desired load cycle. From a practical standpoint, the make-up should be increased slightly above this point so that the coupling will not loosen and uncouple.

The above discussion suggests that the sucker rod designer can maximize the service life of a rod string by controlling the preload achieved during make-up. The Spiralock coupling partially achieves this by using a thread design that yields during make-up. Even with the Spiralock threads, there is an optimum make-up (approximately 1.5) which should not be exceeded. The difference in make-ups of 1.5 and 2.0 is only 9/64-inch of circumferential displacement, little more than one tenth of an inch. Hence, the fatigue life of a sucker rod coupling is very sensitive to the amount of circumferential displacement. From a practical

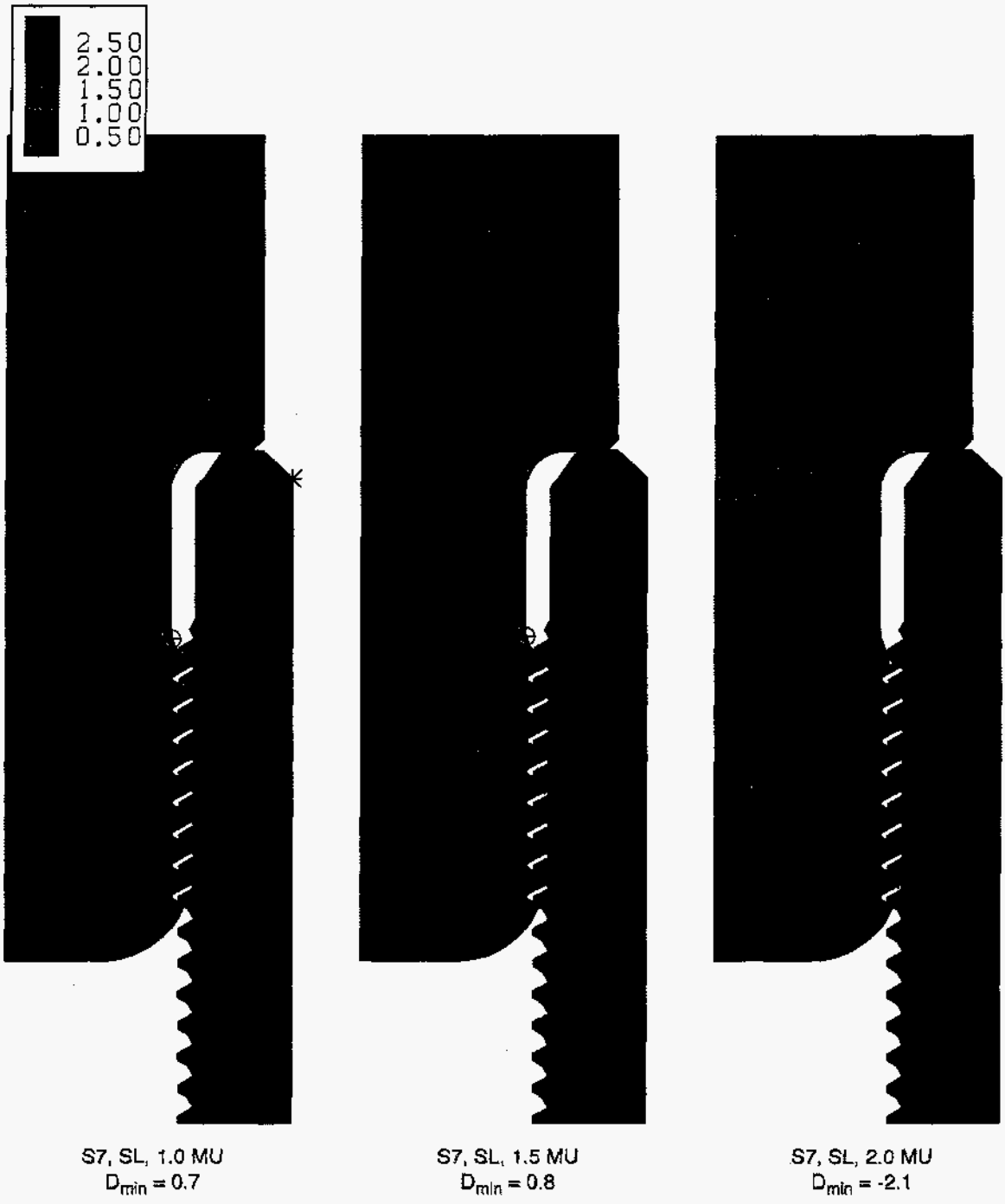

Figure 33. Fatigue safety factor distribution in the 7/8-inch Spiralock coupling (with make-ups of 1.0, 1.5, and 2.0) subjected to the full axial load range (-5 ksi to 40 ksi).

standpoint, it is unreasonable to expect field workers to make-up joints within such tolerances. Even if they could, the Spiralock coupling has another disadvantage. If the coupling is reworked (disassembled and then reassembled), the threads will not yield as much on the second make-up (due to work hardening of the threads) and the preload in the coupling will increase. Hence, the circumferential displacement required to achieve a given preload of the Spiralock coupling will change with each rework. This will be true of any coupling which yields during make-up. A more repeatable solution for controlling coupling preload could be obtained by using crushable steel washers between the box and the pin shoulder. The high strength steel used for the pin and box sections is necessary for fatigue resistance. A steel washer would be necessary to maintain the coupling stiffness. However, a much lower strength steel could be used for the washer since in is always loaded in compression, and, therefore, does not need to be fatigue resistant. The lower yield strength washer will result in a constant crush force for a fairly wide range of circumferential displacements. This way, the coupling preload would not be particularly sensitive to the circumferential displacement. Such a design would allow the optimum preload to be achieved with current API thread forms. Furthermore, the washers could be discarded and replaced should the coupling need to be reworked.

4 Conclusions and Recommendations

The response of a variety of sucker rod couplings to an applied axial load was simulated using axisymmetric finite element models. The sucker rod geometries included the 3/4, 7/8, and 1-inch API (American Petroleum Institute) standard couplings. Various combinations of the slimhole, Spiralock, and Flexbar modifications to the 7/8-inch coupling were investigated, resulting in a total of nine simulated geometries. In addition, the effect of various make-ups (assembly tightness) on the performance of the 7/8-inch API standard and 7/8-inch Spiralock couplings was investigated, resulting in a total of 16 simulations. The make-up process, based on measured circumferential displacement of the coupling from a hand-tight position, was simulated by including a section of an axially expanding material in the box section which, when heated, produced the desired mechanical interference which would result from making-up of the coupling. After make-up, an axial load was applied to the sucker rod ranging from -5 ksi to 40 ksi, encompassing three load cycles identified on a modified Goodman diagram as acceptable for indefinite service life of the sucker rods. Two cycles of the -5 ksi to 40 ksi load cycle were applied to assure that the coupling response was elastic. The constitutive response of the API Grade C steel to the applied loads included both elastic and plastic response.

All of the simulations exhibited some yielding during the make-up process and in the first application of the maximum compression and tensile loads, generally in the pin neck, shoulder, and threads. Yielding on the first load cycle reduced the preload in the coupling which was obtained after make-up. Hence, the preload in a given coupling is a function of the extreme loads it is subjected to. After the initial yielding during make-up and in the first compression and tension cycles, the coupling responds elastically throughout the entire load cycle. Although the sucker rod stresses were, by design, within the envelope of the modified Goodman diagram, the local stresses in the couplings were clearly outside of this envelope for all three load cycles, indicating that all of the simulated couplings would have a finite life.

The simulations of the various coupling geometries and make-ups were compared with respect to how well they accomplish the two primary objectives of preloading threaded couplings: (1) to lock the threaded coupling together so that it will not loosen and eventually uncouple, and (2) to improve the fatigue resistance of the threaded connection by reducing the stress amplitude in the coupling when subjected to cyclic loading. Evaluation of the first objective, locking the threaded coupling, was relatively simple. A coupling will remain locked as long as the mating surfaces of the pin and box sections remain in compression, resisting rotational motion or loosening. Determining how well the various couplings satisfy the second objective, fatigue resistance, was considerably more difficult. This evaluation was accomplished in two parts: nominally and locally. In the nominal evaluation, a set of equations based on the gross dimensions of the coupling were derived which describe how a load applied to a sucker rod is distributed throughout a preloaded coupling. A percentage of the load reduces the compression between the pin and box sections, while remainder increases the tension in the pin section. The later portion, termed the pin partitioning factor, is proportional to the stiffness of the box section of the coupling. A smaller pin partitioning factor reduces the nominal stress amplitude in the pin section and, hence, improves its fatigue resistance. Once a coupling separates, all of the applied load is carried by the pin and the pin partitioning factor increases to a maximum of one. Hence, fatigue resistance is maximized if

the coupling remains locked. The relative stiffness of the pin and box sections is, in general, proportional to their cross-sectional areas. The results of the finite element simulations, in terms of nominal load distribution, agreed well with the nominal load distribution equations.

The local fatigue evaluation characterized the fatigue performance of the various couplings using the local stresses predicted in the finite element simulations and a stress equivalencing criterion for multiaxial stress states. This criterion is based on Sines' equivalent stress theory which states that the permissible effective alternating stress is a linear function of the mean hydrostatic stress. The fatigue damage criterion identified three locations with a high potential for fatigue failure: the pin neck, the root of the first engaged pin thread, and the root of the last engaged box thread. All three locations correspond to the locations of failures observed in field units. Perhaps the most significant finding in this part of the study was the characterization of the coupling parameters which affect the two controlling stress measures of the fatigue criterion. The mean hydrostatic stress, which determines the permissible effective alternating stress, is a function of the coupling make-up. Whereas, the effective alternating stress is a function of the relative stiffness of the pin and box sections of the coupling. As long as the coupling does not separate, the alternating effective stress is unaffected by the amount of circumferential displacement applied during make-up. The local and nominal evaluations were consistent in that the local effective alternating stress amplitudes were proportional to the pin load partitioning factors calculated using the nominal stress equations. These findings suggest three approaches to improving the fatigue resistance of sucker rod couplings.

- *Decrease the nominal alternating stress amplitude by increasing the box stiffness relative to the pin stiffness.* This could be accomplished by either increasing the outside diameter of the box section or by decreasing the pin diameter. The later approach could be taken in instances where well bore clearance is tight. In addition to reducing the nominal stress amplitudes in the pin, a larger box cross-section will reduce the nominal stress amplitude near the last engaged box thread. Demonstrating the effects of relative stiffness, the slimhole coupling, which has a smaller diameter box section, is less stiff than the standard API coupling. As a result, the finite element simulations exhibited a larger nominal load amplitude in the slimhole coupling as well as larger local alternating effective stresses.

- *Optimize the preload generated during the make-up process to minimize the local mean hydrostatic stress in the coupling.* The preload in a coupling needs to be large enough to lock the coupling and avoid the high effective stress amplitudes associated with coupling separation. Additional preload serves only to increase the local mean hydrostatic stresses and decrease the service life of the coupling. The Spiralock coupling partially accomplishes this optimization by incorporating a thread design which yields extensively during make-up, reducing the preload generated in a standard API make-up. As a result, the local mean hydrostatic stresses are considerably smaller in the Spiralock coupling than they are in the API coupling. The analyses demonstrated that the optimum make-up for the Spiralock coupling was approximately one and a half times the standard API make-up. Hence, achievement of an optimum preload still depends on assembler skill. Perhaps a more effective and repeatable method for controlling preload would be to use a crushable steel washer between the pin and box sections.

- *Decrease the severity of the stress concentrations which provide preferred sites for fatigue damage*. This approach was taken in designing the Flexbar modification to the standard API coupling. The results of the Flexbar simulations indicate that this modification was successful in reducing both the mean hydrostatic and effective alternating stresses in the pin neck, extending the service life of the coupling with respect to failure at this location.

Any combination of the above design approaches could be used to extend the service lives of existing sucker rod couplings, or to design a coupling which would meet the desired requirement of indefinite service life.

The local fatigue damage criterion used in this study provided a format for identifying regions with a high potential for fatigue damage and for comparing the fatigue performance of the various coupling geometries and make-ups. If fatigue data was available, this local fatigue damage criterion could have been used to perform service life estimates of the various couplings and make-ups. Consideration should be given to performing multiaxial fatigue tests which could validate this criterion and be used to estimate service lives of sucker rod couplings.

References

1 J. H. Biffle, M. L. Blanford, "JAC2D — A Two-Dimensional Finite Element Computer Program for the Nonlinear Quasi-Static Response of Solids with the Conjugate Gradient Method," Internal Report SAND93-1891, Sandia National Laboratories, Albuquerque, NM, May 1994.

2 J. W. Waggoner, R. G. Buchheit, "Analysis of Sucker Rod and Sinkerbar Failures," Southwestern Petroleum Short Course, pp.124-141, 1993.

3 J. E. Shigley and L. D. Mitchell, "Mechanical Engineering Design," Fourth Edition, McGraw Hill, New York, 1983.

4 "Fatigue Design Handbook," Second Edition, Society of Automotive Engineers, 1988.

5 J. M. Barsom and S. T. Rolfe, "Fracture and Fatigue Control in Structures, Applications of Fracture Mechanics," Second Edition, Prentice-Hall, Inc., 1987.

6 H. E. Boyer, "Atlas of Fatigue Curves," American Society for Metals, 1986.

7 H. O. Fuchs and R. I. Stephens, "Metal Fatigue in Engineering," John Wiley & Sons, 1980.

8 G. Sines, "Metal Fatigue," McGraw-Hill, 1959.

9 G. Sines, "Failure of Metals Under Combined Repeated Stresses with Superimposed Static Stresses," NACA Tech. Note 3495, 1955.

Distribution

MS0328	2674	C. F. Briner
MS0899	4916	Technical Library
MS0701	6100	R. W. Lynch
MS0705	6116	R. P. Cutler (100)
MS0705	6116	M. C. Walck
MS9018	8940-2	Central Technical Files
MS0841	9100	P. J. Hommert
MS0841	9101	T. C. Bickel
MS0833	9103	J. H. Biffle (Route to 9111 & 9115)
MS0834	9112	A. C. Ratzel (Route to 9112 & 9113)
MS0836	9116	C. W. Peterson (Route to 9114 & 9116)
MS0443	9117	J. G. Arguello
MS0443	9117	S. N. Burchett
MS0443	9117	E. L. Hoffman (10)
MS0443	9117	H. S. Morgan (Route to 9117 & 9118)
MS0443	9117	C. M. Stone
MS0443	9117	G. W. Wellman
MS0443	9117	QA File
MS0437	9118	C. R. Adams
MS0828	9104	R. K. Thomas
MS0439	9234	D. R. Martinez (Route to staff)
MS0619	12690	Review and Approval Desk for DOE/OSTI